Astronomy & Astrophysics manuscript no. Colzietal.2017-ArXiv
September 14, 2017

Nitrogen and hydrogen fractionation in high-mass star forming cores from observations of HCN and HNC

L. Colzi[1,2], F. Fontani[2], P. Caselli[3], C. Ceccarelli[4,5], P. Hily-Blant[4,5], and L. Bizzocchi[3]

[1] Università degli studi di Firenze, Dipartimento di fisica e Astronomia, Via Sansone, 1 -50019 Sesto Fiorentino (Italy)
[2] INAF-Osservatorio Astrofisico di Arcetri, Largo E. Fermi 5, I-50125, Florence, Italy
[3] Max-Planck-Institüt für extraterrestrische Physik, Giessenbachstrasse 1, D-85748, Garching bei München, Germany
[4] CNRS, IPAG, F-38000 Grenoble (France)
[5] Univ. Grenoble Alpes, IPAG, F-38000 Grenoble (France)

Received date; accepted date

ABSTRACT

The ratio between the two stable isotopes of nitrogen, ^{14}N and ^{15}N, is well measured in the terrestrial atmosphere ($\sim$ 272), and for the pre-Solar nebula ($\sim$ 441, deduced from the Solar wind). Interestingly, some pristine Solar System materials show enrichments in ^{15}N with respect to the pre-Solar nebula value. However, it is not yet clear if, and how, these enrichments are linked to the past chemical history, due to the limited number of measurements in dense star-forming regions. In this respect, dense cores believed to be precursors of clusters containing also intermediate- and high-mass stars are important targets, as the Solar System was probably born within a rich stellar cluster. The number of observations in such high-mass dense cores has remained limited so far. In this work, we show the results of IRAM-30m observations of the J=1-0 rotational transition of the molecules HCN and HNC, and their ^{15}N-bearing counterparts, towards 27 intermediate/high-mass dense cores divided almost equally in three evolutionary categories: high-mass starless cores, high-mass protostellar objects, and ultra-compact HII regions. We have also observed the DNC(2-1) rotational transition, in order to search for a relation between the isotopic ratios D/H and ^{14}N/^{15}N. We derive average ^{14}N/^{15}N ratios of 359$\pm$16 in HCN and of 438$\pm$21 in HNC, with a dispersion of about 150-200. We find no trend of the ^{14}N/^{15}N ratio with the evolutionary stage. This result agrees with what found from N_2H^+ and its isotopologues in the same sources, although the ^{14}N/^{15}N ratios from N_2H^+ show a dispersion larger than that in HCN/HNC. Moreover, we have found no correlation between D/H and ^{14}N/^{15}N in HNC. These findings indicate that: (1) the chemical evolution does not seem to play a role in the fractionation of nitrogen; (2) the fractionation of hydrogen and nitrogen in these objects are not related.

1. Introduction

Nitrogen is the fifth most abundant element in the Universe. It possesses two stable isotopes, ^{14}N and ^{15}N. Füri & Marty (2015) proposed that there are three distinct isotopic reservoirs in the Solar system: the protosolar nebula, the inner Solar system and cometary ices. In the terrestrial atmosphere (TA), the typical isotopic ratio ^{14}N/^{15}N, as derived from N_2, is $\sim$272 (Marty et al. 2009). This value is almost a factor two larger than the ratio measured in nitrile-bearing molecules and in nitrogen hydrides of some comets (e.g. $\sim$150, Manfroid et al. 2009, Shinnaka et al. 2016), and larger of even a factor five in carbonaceus chondrites (e.g. $\gtrsim$50, Bonal et al. 2009). On the other hand, the ratio measured in Solar wind particles collected by the Genesis spacecraft, representative of the proto-Solar nebula value (PSN) and similar to that measured on Jupiter (Owen et al. 2001), is 441$\pm$6 (Marty et al. 2010). Thus, the PSN ^{14}N/^{15}N value is about 2 times larger than the TA value and 3 times larger than the value measured in comets. These measurements suggest that multiple isotopic reservoirs were present very early in the formation process of the solar system. This was recently demonstrated based on the CN/C^{15}N and HCN/HC^{15}N isotopic ratios measured in a sample of PSN analogs (Hily-Blant et al. 2017). The nature and origin of these reservoirs remain, however, elusive. Currently, the two main possibilities are i) isotope-selective photodissociation of N_2 in the PSN by stellar UV (Heays et al. 2014, Guzman et al. 2017), and ii) an interstellar origin by mass fractionation reaction (Hily-Blant et al. 2013b, Roueff et al. 2015). A similar isotopic enrichment in comets, some meteorites, and Interplanetary Dust Particles with respect to the PSN value has been found also for hydrogen. In the PSN, the D/H ratio is $\sim10^{-5}$ (Geiss et al. 1998), i.e. similar to the cosmic elemental abundance (Linsky et al. 2006). In comets, different values of the D/H ratio were estimated: in the Jupiter family comet 67P/Churyumov-Gerasimenko the D/H ratio measured in H_2O is about 5×10^{-4}, approximately three times that of Earth's oceans (Altwegg et al. 2015), and other results, from Herschel, have shown D/H$\sim$ 1.5×10^{-4} in another Jupiter family comet 103P/Hartley (Hartogh et al. 2011) same as the Earth's ocean. In carbonaceous chondrites, values of D/H$\sim$1.2-2.2$\times10^{-4}$ in hydrous silicates were obtained (Robert 2003). Furthermore, very high D/H ratios of $\sim10^{-2}$ (Remusat et al. 2009) have been found in small regions in Insoluble Organic Matter (IOM) of meteorites and Interplanetary Dust Particles (IDPs), called "hot spots". Deuterium fractionation in the Interstellar Medium and in the Solar System objects was also discussed by Ceccarelli et al. (2014).

From a theoretical point of view, for several species the D/H enhancement has its origin in a low-temperature environment where ion-molecule reactions are favoured, starting from the reaction:

$$H_3^+ + HD \rightarrow H_2D^+ + H_2 + 232K,$$

which produces an enhanced H_2D^+/H_3^+ abundance ratio, for temperatures lower than $\sim$50 K and when H_2 is mainly in para form (e.g. Pagani et al. 1992; Gerlich et al 2002; Walmsley et al. 2004). Moreover, in dense cores, where CO freezes-out on dust grains (e.g. Caselli et al. 1999, Fontani et al. 2012),

H_2D^+ can survive and H_2D^+/H_3^+ is further enhanced causing a high level of deuteration in molecules. The role of grain surface chemistry on icy material during the early cold phase is also expected to play an important role for the deuteration of neutral species like water, formaldehyde, methanol and complex organic molecules (e.g. Cazaux et al. 2011, Taquet et al. 2012, 2013). This is due to the fact the enhanced abundances of the deuterated forms of H_3^+ (H_2D^+, D_2H^+, D_3^+) produce enhanced abundances of D atoms in the gas phase, upon their dissociative recombination with electrons. The enhanced D abundance implies a larger D/H ratio, so that unsaturated molecules on the surface (in particular CO) can be deuterated as well as hydrogenated to produce singly and doubly deuterated water and formaldehyde as well as singly, doubly and triply deuterated methanol (e.g. Caselli & Ceccarelli 2012; Ceccarelli et al. 2014).

In principle, similar gas-phase mass fractionation reactions can also produce ^{15}N enrichments under cold and dense conditions. This motivated the search for correlated enrichments in D and ^{15}N in cosmomaterials (Aléon et al. 2009) although chemical models suggest that such correlations may not be present (Wirström et al. 2012). Furthermore, while the above scenario of D-enrichments through ion-neutral mass fractionation reactions has been proved firmly for D through observations of low- and high-mass star-forming regions (e.g. Crapsi et al. 2005, Caselli et al. 2008, Emprechtinger et al. 2009, Fontani et al. 2011), the reasons for ^{15}N enrichment are still highly uncertain. For example, HC^{15}N and H^{15}NC could be formed through the dissociative recombination of HC^{15}NH$^+$: in fact, Terzieva & Herbst (2000) found that the reaction that causes the most of N-fractionation is the exchange reaction between ^{15}N and $HCNH^+$:

$$^{15}N + HCNH^+ \rightarrow N + HC^{15}NH^+ + 35.1K,$$

but they assumed that this reaction could occur without an energy barrier. The most recent and complete chemical models (Roueff et al. 2015) are implementend with the recent discovery that this reaction have an energy barrier and indicate that ^{15}N should not be enriched during the evolution of a star-forming core, not even at the very early cold phases. Moreover, the observational works devoted to test these predictions are still very limited.

In the few low mass pre-stellar cores or protostellar envelopes observed so far, values of $^{14}N/^{15}N$ comparable to the value of the PSN have been measured from N_2H^+ and NH_3 (330±150 in N_2H^+, Daniel et al. 2016; 350 - 500, Gerin et al. 2009; 334±50, Lis et al. 2010 in NH_3), or even larger (1000±200 in N_2H^+, Bizzocchi et al. 2013). Conversely, through observations of the nitrile-bearing species HCN e HNC in low-mass sources, the $^{14}N/^{15}N$ ratio turns out to be significantly lower (140 - 360, Hily-Blant et al. 2013a; 160-290, Wampfler et al. 2014). Moreover low values have been recently found also in protoplanetary disks (from 80 up to 160, Guzmán et al. 2017), but this results are based on a low statistics (six protoplanetary disks). From the point of view of chemical models, differential fractionation is expected between nitriles and hydrides (Wirström et al. 2012, Hily-Blant et al. 2013a, 2013b), although the most recent models (Roueff et al. 2015) do not support this scenario. However, none of these models is able to reproduce the low fractionation observed in N_2H^+ towards L1544 (Bizzocchi et al. 2013) and the large spread in Fontani et al. 2015a.

To investigate the possible correlation between D and ^{15}N enrichments in interstellar environments, Fontani et al. (2015a) conducted a survey of the $^{14}N/^{15}N$ and D/H isotopic ratios towards a sample of high-mass cores in different evolutionary stages and found a possible anticorrelation, which, however, was quite faint and obtained from a low number (12 objects) of detections. In addition, no correlation between the disk averaged D/H and $^{14}N/^{15}N$ ratios have been measured by Guzmán et al. (2017) in six protoplanetary disks, but again the conclusion is based on a poor statistics. Another intriguing result is that the D- and ^{15}N-enhancements are not always observed in the same place in pristine Solar System material (Busemann et al. 2006; Robert & Derenne 2006). Therefore, it is important to gather more data in sources that are good candidates to represent the environment in which our Sun was born to put stringent constraints on current chemical models. In this respect, intermediate- and high-mass star-forming cores are interesting targets because growing evidence is showing that the Sun was born in a rich cluster, containing also massive stars (Adams 2010, Banerjee et al. 2016). Moreover, Taquet et al. (2016) have recently proposed that the proto-Sun was born in an environment denser and warmer than that usually considered as a Solar System progenitor. In any case, because the statistic is still poor, having more observations in star-forming cloud cores in different evolutionary stages is useful to better understand if and how the ^{15}N fractionation process is eventually influenced by evolution. An example of existing work about ^{15}N fractionation in high-mass dense cores is this of Adande & Ziurys (2012). This work have a larger beam with respect to that used in our observations and they do not have an evolutionary classification of the sources, so their results are difficult to be interpreted in an evolutionary study.

In this work we report the first measurements of the $^{14}N/^{15}N$ ratio derived from HCN and HNC in a sample of 27 dense cores associated with different stages of the high-mass star formation process, and already studied in deuterated molecules and in the ^{15}N-bearing species of N_2H^+ (Fontani et al. 2011, 2015a, 2015b). In particular, Fontani et al. (2015a) have measured, for the first time, the $^{14}N/^{15}N$ isotopic ratio in N_2H^+ towards the same sources. Therefore, these new data allow us to investigate the possible difference between nitrogen hydrides and nitrile-bearing species proposed by both theoretical studies (Wirström et al. 2012) and observational findings (Hily-Blant et al. 2013a). We report also measurements of the D/H ratios for HNC, to search for relations between the two isotopic ratios.

2. Observations

We performed observations of the J=1-0 rotational transition of H^{15}NC, HN^{13}C, HC^{15}N and H^{13}CN towards the 27 sources observed by Fontani et al. (2015a) from 6 to 9 June, 2015, using the 3 mm receiver of the IRAM-30m telescope. We refer to this paper for the description of the source sample. We simultaneously observed the J=2-1 transition of DNC with the 2 mm receiver. Table 1 presents the observed spectral windows and some main technical observational parameters. Table 2 presents the hyperfine frequencies of H^{13}CN. The atmospheric conditions were very stable during the whole observing period, with precipitable water vapour usually in the range 3 – 8 mm. The observations were made in wobbler-switching mode with a wobbler throw of 240". Pointing was checked almost every hour on nearby quasars, planets, or bright HII regions. The data were calibrated with the chopper wheel technique (see Kutner & Ulich 1981), with a calibration uncertainty of about 10% . The spectra were obtained in antenna temperature units, T_A^*, and then converted to main beam brightness temperature, T_{MB}, via the relation $T_A^* = T_{MB}(B_{eff}/F_{eff}) = T_{MB}\eta_{MB}$, where $\eta_{MB} = B_{eff}/F_{eff}$ is the ratio between the Main Beam efficiency (B_{eff}) of the telescope and the Forward efficiency of the telescope (F_{eff}). The spectra were obtained with the fast Fourier transform spectrom-

Table 1. Line rest frequencies and observational parameters

Line	Frequency GHz	HPBW arcsec	Δv^* km s^{-1}	T_{sys} K	η_{MB}	F_{eff}
HC^{15}N(1-0)	86.0549	28	~ 0.16	100–150	0.85	0.95
H^{13}CN(1-0)	86.3399	28	~ 0.16	100–150	0.85	0.95
HN^{13}C(1-0)	87.0908	28	~ 0.16	100–150	0.85	0.95
H^{15}NC(1-0)	88.8657	27	~ 0.16	100–150	0.84	0.95
DNC(2-1)	152.60977	15	~ 0.096	200–250	0.78	0.93

*: velocity resolution of the spectrum.

Table 2. Frequencies of the hyperfine components of the transition H^{13}CN(1-0). F is the quantum number associated with the sum between the orbital angular momentum |J| and the ^{14}N nuclear angular momentum. The hyperfine spitting due to ^{13}C is negligible.

J'-J"	F'-F"	Frequency (GHz)
1-0	1-1	86.33873
	2-1	86.34016
	0-1	86.34225

eters with the finest spectral resolution (FTS50), providing a channel width of 50 kHz. All calibrated spectra were analysed using the GILDAS[1] software developed at the IRAM and the Observatoire de Grenoble. Baselines in the spectra were all fitted by constant functions, or polynomials of order 1. The rest frequencies used for the line identification, have been taken from different laboratory works: HC^{15}N from Cazzoli et al. (2005), H^{13}CN from Cazzoli & Puzzarini (2006), HN^{13}C from van der Tak et al. (2009), H^{15}NC from Pearson et al. (1976) and DNC from Bechtel et al. (2006). The other spectroscopic parameters used in the derivation of the column densities have been taken from the Cologne Molecular Database for Spectroscopy[2] (CDMS; Müller et al. 2001, 2005) except for H^{15}NC, for which we have used the Jet Propulsion Laboratory database[3].

3. Results

3.1. H^{15}NC, HN^{13}C, HC^{15}N and H^{13}CN

The H^{15}NC(1-0) line has been detected in 26 cores (96.3%): 11 HMSCs, 8 HMPOs and 7 UC HIIs; the HC^{15}N(1-0) line has been detected in 24 cores (88.8%): 8 HMSCs, 9 HMPOs and 7 UC HIIs; the HN^{13}C(1-0) line is detected in all sources (100%) and also the H^{13}CN(1-0) line is clearly detected in all sources (100%).

First of all, to evaluate the isotopic ratios we have used the ^{13}C-bearing species of HCN and HNC because the main isotopologues are usually optically thick (e.g. Padovani et al. 2011). Then, we can derive the ^{14}N/^{15}N ratio by correcting for the ^{12}C/^{13}C ratio. This latter has been derived from the relation between this ratio and the source galactocentric distance found for CN by Milam et al. (2005). Galactocentric distances have been taken from Fontani et al. (2014, 2015a).

Both H^{15}NC(1-0) and HC^{15}N(1-0) do not have hyperfine structure, then all the lines were fitted with a single Gaussian. On the contrary, HN^{13}C(1-0) and H^{13}CN(1-0) have hyperfine structure. This cannot be resolved for the HN^{13}C(1-0) because the line widths are always comparable to (or larger than) the separation in velocity of the hyperfine components. Then all the lines were fitted with single Gaussians too, and since the column densities will be derived from the total integrated area of the rotational line, this simplified approach will not affect our measurements as long as the lines are optically thin, which is discussed in this Section. On the other hand, it can overestimate the intrinsic line width. To estimate of how much, we have fitted a line both with the Gaussian and the hyperfine method, and we have found that with a single Gaussian, the line width is about 30% larger than that obtained with the hyperfine structure.

Moreover, the fit using the hyperfine method have demonstrated that the lines are optically thin. Finally, for H^{13}CN(1-0), for which we could resolve the hyperfine structure, we fitted the components simultaneously assuming that they have the same excitation temperature (T_{ex}) and line width, and that the separation in velocity is fixed to the laboratory value. This fitting procedure gave us good results in all spectra. The Gaussian fitting results are listed in Tab. A.1 and A.2 and the hyperfine fitting results are listed in Tab. A.3. In Fig. B.1, B.2, B.3 and B.4 we show the spectra of the H^{15}NC, HC^{15}N, HN^{13}C and H^{13}CN(1-0) lines for all the 27 sources. As can be noted, the hyperfine components of H^{13}CN(1-0) were always detected. The spectra of AFGL5142-EC may be partially contaminated from the nearby core AFGL5142-mm, but this emission is expected to be not dominant because the angular separation between the two cores is 30" (Busquet et al. 2011), equal than the beam of the telescope.

The total column densities of the four species, averaged within the beam, have been evaluated from the total line integrated intensity using eq. (A4) of Caselli et al. (2002), which assumes that T_{ex} is the same for all transitions within the same molecule, and optically thin conditions. The assumption of optically thin lines is justified by the fact that from all the hyperfine fits of H^{13}CN(1-0) we find $\tau \ll 1$ and well constrained ($\Delta\tau/\tau \leq 1/3$). We assume that also the lines of the other isotopologues are optically thin. We assume LTE conditions, as all the observed sources have average H_2 volume densities of the order of $\sim 10^5$ cm^{-3} (see Fontani et al. 2011 and references therein), i.e. comparable or marginally smaller than the critical densities of the lines observed, thus this assumption is also reasonable. Because the T_{ex} cannot be deduced from our optically thin spectra (and cannot deduced T_{ex} also because we have only one transition), we adopted as T_{ex} the kinetic temperatures given by Fontani et al. (2011), who derived them following the method described in Tafalla et al. (2004) based on Monte Carlo models from which is obtained a relation among the kinetic temperature, T_k, and the NH_3 rotation temperature between metastable levels. The T_k values are given in the last column of Table 3 and 4. This last assumption is critical for the single column densities, but the HN^{13}C/H^{15}NC and H^{13}CN/HC^{15}N column density ratios do not change significantly by varying T_k between 20 and 100 K: changes are of one per cent or of ten per cent depending on the source. All the column densities and the parameters used to derive them (line integrated intensities) are given in Tables 3 and Tab. 4. We consider as detections the lines with $T_{MB}^{peak} \geq 3\sigma$. For the lines not clearly detected, we have distinguished between those with a $2.5\sigma \leq T_{MB}^{peak} < 3\sigma$, and those with $T_{MB}^{peak} < 2.5\sigma$. For the first ones, considered as tentative detections, we have computed the total column densities as explained above, and for the latter ones we have given an upper limit to the integrated

[1] The GILDAS software is available at http://www.iram.fr/IRAMFR/GILDAS
[2] http://www.astro.uni-koeln.de/cdms
[3] https://spec.jpl.nasa.gov/

areas, and hence to the total column densities using:

$$\int T_{MB}\, dv = \frac{\Delta v_{1/2} T_{MB}^{peak}}{2\sqrt{\frac{ln2}{\pi}}},$$

where σ is the r.m.s. of the spectra, T_{MB}^{peak} is taken equal to 3σ and $\Delta v_{1/2}$ is the average value of the FWHM of the lines clearly detected for the corresponding transition and evolutionary stage of the source. The average value $\Delta v_{1/2}$ for the high-mass starless cores in our data is $\Delta v_{HMSC} = 2.2 \pm 0.3$ km/s, while for the high-mass protostellar objects is $\Delta v_{HMPO} = 1.8 \pm 0.2$ km/s. Finally we have derived the column density uncertainties from the errors on the line areas for optically thin lines, given by $\sigma \times \Delta v \times \sqrt{N}$ (σ= root mean square noise in the spectrum, Δv= spectral velocity resolution, N= number of channels with signal) and taking into account the calibration error (10%) for the T_{MB}. Conversely, uncertainties in the $^{14}N/^{15}N$ ratios have been computed from the propagation of errors on the column densities, as explained above, without taking the calibration uncertainties into account because the lines were observed in the same spectrum (see Sect. 2), so that the calibration error cancels out in their ratio.

3.2. DNC

We have also detected the rotational transition DNC(2-1) for all the 27 sources. These lines will be used to measure the D/H ratio, that will be compared with the $^{14}N/^{15}N$ ratio. Such a high detection rate indicates that deuterated gas is present at every stage of the massive star and star cluster formation process, as it has already been noted by Fontani et al. (2011). The transition possesses a hyperfine structure that, because of the broad line widths (see Table A.2), is not resolved. Therefore, the lines where fitted with a single Gaussian. To estimates how much the line widths are overestimated using Gaussian fits, we have fitted a line both with the Gaussian and the hyperfine method, and we have found that with a single Gaussian, the line width is about 10% larger than that obtained with the hyperfine structure. We point out that for evolved sources (HMPOs and UC HIIs) there is another line in the spectra partly overlapping with DNC(2-1), identified as acetaldehyde at 152.608 GHz (the $J_{Ka,Kc} = 8_{0,8}$-$7_{0,7}$ transition). The fact that the line is detected only in the evolved objects is consistent with the idea that acetaldehyde is probably released from grain mantles because it is detected only in the warmer and more turbulent objects (see e.g. Codella et al. 2015). When we have fitted the DNC lines with Gaussians, we have excluded the contribution of this line by fitting the two lines simultaneously and when possible we have just excluded this line from the fit. Fitting results are in Tab. A.2.

Also in this case we have determined the column densities under the assumption of optically thin conditions and same T_{ex} for all transitions using eq. (A4) of Caselli et al. (2002):

$$N_{TOT} = \frac{8\pi\nu_{ij}^3}{c^3 A_{ij}} \frac{1}{g_i} \frac{W}{(J_{\nu_{ij}}(T_{ex}) - J_{\nu_{ij}}(T_{BG}))} \frac{1}{\left(1 - \exp(-\frac{h\nu_{ij}}{kT_{ex}})\right)} \frac{Q(T_{ex})}{\exp(-\frac{E_j}{kT_{ex}})} \quad (1)$$

where ν_{ij} is the frequency of the transition, A_{ij} is the Einstein coefficient of spontaneous emission, g_i is the statistical weight of the upper level, E_j is the energy of the lower level, c is the speed of light, k is the Boltzmann constant, T_{ex} is the excitation temperature of the transition, $Q(T_{ex})$ is the partition function at temperature T_{ex}, and T_{BG} is the background temperature (2.7 K), $J_{\nu_{ij}}(T)$ is

$$J_{\nu_{ij}}(T) = \frac{h\nu_{ij}}{k} \frac{1}{\exp(\frac{h\nu_{ij}}{kT}) - 1},$$

W is the integrated intensity of the line ($\int T_B\, dv = (\int T_{MB}\, dv)\frac{\Omega_{MB}}{\Omega_s}$, where T_B is the brightness temperature, Ω_{MB} is the solid angle of the main beam, and Ω_s is the solid angle of the source). However, in this case the HNC/DNC ratio depends on the temperature because of the different excitation conditions of the two transitions observed ((2–1) for DNC and (1–0) for $HN^{13}C$), so that the ratio depends on the temperature by the factor $\exp(E_j/kT)$. We had also to correct the HNC/DNC ratios for the different beam of the antenna at the frequencies of the two lines and we have assumed that the emissions of DNC(2-1) and HNC(1-0) are less extended than the beam size of DNC(2-1). This last correction results in a factor 3.09 to be multiplied to the HNC/DNC ratio:

$$\left(\frac{1.22\frac{\lambda_1}{D}}{1.22\frac{\lambda_2}{D}}\right)^2 = \left(\frac{\lambda_1}{\lambda_2}\right)^2 = \left(\frac{\nu_2}{\nu_1}\right)^2 = 3.09$$

where λ_1 and λ_2 are the wavelenghts of the HNC(1-0) and DNC(2-1) transitions, respectively (and ν_1 and ν_2 the corresponding frequencies). In Fig. B.5, the spectra of DNC(2-1) for all the 27 sources are shown. The total column densities are listed in Tab. 3. Finally we have derived the errors as explained in Sect. 3.1, but here for the D/H ratios we have considered also the calibration uncertainties because the two lines were observed in separate setups.

4. Discussion

4.1. ^{15}N-Fractionation

The comparison between the column densities of the ^{15}N-containing species and those of their main isotopologues, derived as explained in Sect. 3, is shown in Fig. 1. The corresponding $^{14}N/^{15}N$ ratios are given in Tab. 3 and in Tab. 4.

Let us first discuss the ^{15}N-fractionation found for HCN. As we can see from the top left panel in Fig. 1, there is not a large spread of measured values, which are very close to the value found for the PSN. The mean values for the three evolutionary stages are: 346±37 for HMSCs, 363±25 for HMPOs and 369±25 for UC HIIs. Therefore, although the HMSCs have the highest ^{15}N-enrichment, the mean values for the three evolutionary categories are consistent within the errors, which indicates that time does not seem to play a role in the fractionation of nitrogen (at least until the formation of a HII region). In the top panels of Fig. 2 the $^{14}N/^{15}N$ ratios calculated for HCN in the 27 sources are shown as a function of the Galactocentric distance, of the line width, and of the kinetic temperature, respectively: again, there is no evidence of a trend of these ratios with any of the parameters adopted. In particular, the lack of correlation with both temperature and line width, thought to increase both with the evolution of the source, confirms the independence between the $^{14}N/^{15}N$ ratio with the core age. The lack of correlation with evolutionary parameters was found also by Fontani et al. (2015a) in N_2H^+, but the dispersion of the ratios is clearly much smaller in our study (from 180 up to 1300 in Fontani et al. 2015a and from 250 up to 650 in this work). This may also be due to the fact that they have on average larger uncertainties.

Let us examine now the ^{15}N- fractionation found for HNC: also here we do not find a large spread of values, if compared with that found in Fontani et al. (2015a). In fact, the ^{14}N/^{15}N ratios are distributed within $\sim$ 250 and 630 (top-right panel in Fig. 1). The mean values for the three evolutionary stages are: 428±40 for HMSCs, 462±31 for HMPOs and 428±29 for UC HIIs, namely consistent within the errors with the ^{14}N/^{15}N ratio measured for the PSN of about 441 (from the Solar wind). Also for this molecule it was not found a trend between the isotopic ratio and either the line width or the kinetic temperature (bottom panels of Fig. 2). In conclusion, for both ratios, time does not seem to play a role.

The lack of correlation between the ^{14}N/^{15}N isotopic ratios and evolutionary parameters or physical parameters (FWHM, T_k) are somewhat consistent with the chemical model of Roueff et al. (2015) who predict no fractionation of HCN and HNC in cold and dense conditions. However, their models are more appropriate to low-mass dense cores, with a T_k of 10 K, than to the warmer high-mass prestellar objects of the type studied in this work. This may explain the lack of carbon fractionation in our work, in constrast to their predictions. In fact we stress that ^{13}C in theory can suffer for possible reduced abundances due to the fact that nitriles and isonitriles are predicted to be significantly depleted in ^{13}C (Roueff et al. 2015). However, this depletion factor is at most a factor 2 (see Fig. 4 in Roueff et al. 2015) and is derived from a chemical model with fixed kinetic temperature of 10 K, which is not the average kinetic temperature of our sources (not even the starless cores, see Table 3). Therefore, the predictions of this model may not be appropriate for our objects. Furthermore, the ^{13}C-fractionation is dependent on the time and temperature evolution (Szűcs et al. 2014, Röllig & Ossenkopf 2013) and observational tests to check whether this theoretical effect is real have yet to be performed.

Intriguingly, doing the Kolmogorov-Smirnov test, a non-parametric statistical test, to check if the two data sets (the first are the HC^{14}N/HC^{15}N ratios and the second are the H^{14}NC/H^{15}NC ratios) belong to the same distributions, we found a P-value=0.078. The test indicates independence only if P $\leq$ 0.05, and this could mean that with our result we can not conclude anything about the dependence or the independence of the two samples. What is known from the literature is that H^{15}NC and HC^{15}N can form through the same reactions (see Terzieva & Herbst 2000 and Wirström et al. 2012). We also have checked the H^{15}NC/HC^{15}N column density ratio and we found that this is roughly more than 1 for HMSCs (with an average value of $\sim$ 1 ± 0.5) and roughly less than 1 for HMPOs and UC HIIs (with an average value of $\sim$ 0.3 ± 0.1). Loison et al. (2014) show that in cold regions, where C and CO are depleted, the dissociative recombination of HCNH$^+$ acts to isomerize HCN into HNC, producing HCN/HNC ratios close to or slightly above one. In hot gas, the CN + H_2 reaction with large activation energy (2370 K; Jacobs et al. 1989) and the isomeration process C + HNC $\rightarrow$ C + HCN (Loison et al. 2014) may be responsible for the large HCN/HNC measured in hot cores (Schilke et al. 1992) and in Young Stellar Objects (Schöier et al. 2002). The fact that our HC^{15}N/H^{15}NC ratios are always close to one appears to imply that both species are probing similar low temperature gas.

Interestingly, the ^{14}N/^{15}N ratio measured towards the source HMSC-G034F2 is an outlier (too high), for the distribution of the ratios in both HCN and HNC (but with large errors compared to other objects): a similar high value was found by Bizzocchi et al. (2013) in L1544 that is a typical low-mass pre–stellar core. In particular, Bizzocchi et al. found a value of ^{14}N/^{15}N$\simeq$1000±200 from the N_2H^+. This result, and those measured in HMSC-G034F2, are not consistent with the predictions of current models on nitrogen chemistry for N_2H^+, HCN and HNC (Roueff et al. 2015, Hily-Blant et al. 2013a). The ^{14}N/^{15}N ratios in HCN and HNC for cores G028-C1, G034-C3, G028-F2, G034-F1, G034-G2 have also been studied indipendently by Zeng et al. (2017) and both works obtain consistent results (within a factor of two). Taking into account HC^{15}N in G028-C1 and comparing our spectrum with that of Zeng et al. (2017) at the same velocity resolution of 0.68 km/s we have obtained a r.m.s of 0.01 K, while they have obtained a r.m.s of 0.02 K. Our T_{MB}^{peak} is 0.03 K that is more than 2.5 σ, so we can refer to this line as a tentative detection, while Zeng et al. (2017) have a r.m.s that is comparable with the peak of our line. They have also derived the upper limit of the column density using a $\Delta v_{1/2}$ of the line of 2 km/s, while with our fit we obtained a $\Delta v_{1/2}$ of 4 km/s: this is the reason for the factor 2 of difference in the integrated area of this line in the two works. This effect is the same in the other spectra (please compare Fig. A1, A2 and A3 of their work with our Fig. B1, B2, B3 and B4), and the different integrated areas are also due to the different resolution and sensitivity.

4.2. D-Fractionation

In the top panel of Fig. 3 the comparison between the column densities of DNC and HNC, derived as explained in Sect. 3, is shown. The N(HNC)/N(DNC) mean values obtained for the three evolutionary stages are: 823±94 for HMSCs, 983±189 for HMPOs and 1275±210 for UC HIIs, indicated by three different lines in Fig. 3. Therefore, the D/H mean ratios are: (1.4±0.2)×10^{-3} for HMSCs, (1.3±0.2)×10^{-3} for HMPOs and (0.9±0.1)×10^{-3} for UC HIIs. The D/H mean values were obtained taking all the D/H values (Tab. 3) and compute for them the average. We note that the D/H values are slightly higher in the early stages, but due to the large dispersions, the differences between the three evolutionary categories are not statistically significant. This result confirms the marginally decreasing trend found by Fontani et al. (2014), derived from the DNC (1–0) transition in a subsample of the sources observed in this work. Fontani et al. (2014) found average D/H of 0.012, 0.009 and 0.008 in HMSCs, HMPOs and UC HIIs, respectively, with no statistically significant differences among the three evolutionary groups.

4.3. Comparison between D/H and ^{14}N/^{15}N ratios

Considering both D- and N-fractionation for HNC toward the same sources, we can find a hint whether the two fractionations are linked. The bottom-right panel in Fig. 1 show HNC/DNC as a function of HNC/H^{15}NC. The data show an independence between the two data sets and this can be shown computing the Kendall τ test. This is a non-parametric test used to measure the ordinal association between two data sets; its definition is:

$$\tau = \frac{(\#\text{ concordant pairs}) - (\#\text{ discordant pairs})}{\frac{n(n-1)}{2}},$$

with n the number of the total pairs. If $\tau = 1$ there is a full correlation, if $\tau = -1$ there is full anticorrelation and if $\tau = 0$ there is independence between the two data sets. We have chosen this statistical test because, compared to other non-parametric tests (i.e. the Spearman's ρ correlation coefficient) this is more robust; moreover, this allows us to compare our analysis with that performed by Fontani et al. (2015a), who used the same test. Following this, we have computed τ for the two data sets:

HNC/DNC and HNC/H^{15}NC and we have found $\tau \sim 0.13$, thus independence between D- and ^{15}N- fractionation in these sources for HNC. This result must be compared with that of Fontani et al. (2015a) that suggested a possible anti-correlation between the two isotopic ratios for N_2H^+. This finding arises mostly from the fact that the ^{14}N/^{15}N ratio does not vary with the core evolution, while the D-fractionation shows a faint decreasing trend. This result indicates that the parameters that cause D-enrichment in HCN and HNC may not influence the fractionation of nitrogen. The independence that we have found reflects what is found in some pristine Solar System material, in which the spots of high D-enrichments are not always spatially coincident with those with high ^{15}N enrichment. From the point of view of the models, as discussed in Wirström et al. (2012), the D- and ^{15}N- enrichments do not need to be spatially correlated (although could be produced by the same mechanism, i.e. exothermic reactions due to the different zero point energy of the heavier isotope), because relevant reactions for D- and ^{15}N- enrichments have different energy barriers. The recent model of Roueff et al. (2015) have reviewed some of the reactions in ^{15}N- fractionation, and concluded that other modeling work is necessary to fully understand the relation of the two fractionation processes.

4.4. Comparison between N(HNC) and N(HCN)

For completeness we have calculated also the ratio between N(HNC) and N(HCN). In Fig. 4 it is shown the column density of HCN versus the HNC one, and we note immediately that HMSCs show values of HCN/HNC$\lesssim$1 unlike HMPOs and UC HIIs, for which the ratio is >1. Mean values are 0.8 ±0.2 for HMSCs, 2.5 ±0.2 for HMPOs and 2.0±0.2 for UC HIIs.

We have computed the HNC/HCN ratio in these two data sets: HMSCs and HMPOs+UC HIIs and using the non-parametric statistical test Kolmogorov-Smirnov we obtain a P-value=0.025, which indicates that the two distributions are different. The work of Schilke et al. (1992) shows predictions and observations for the Orion hot core OMC-1, that is the prototype of a high-mass hot core. They found that the HCN/HNC abundance ratio is very high (∼80) in the vicinity of Orion-KL, but it declines rapidly in adjacent positions to values of ∼5. They compared the observations with the predictions of the molecular cloud chemistry and found agreement with steady state models. More recently Jin et al. (2015) found that the abundance ratio increases if the sources evolved from IRDCs to UC HIIs and they suggested that this can happen for neutral-neutral reactions where HNC is selectively consumed for T$\gtrsim$24 K (Hirota et al. 1998):

HNC + H → HCN + H;

HNC + O → NH + CO.

For the first reaction it was found a 2000 K barrier and for the second there is not yet been theoretical and experimental studies but if it is possible N(HNC)/N(HCN) would decrease rapidly in warm gas. Therefore we emphasize the importance of future laboratory measurements of these latest reactions, especially at low temperatures.

4.5. Comparison with the $^{14}N/^{15}N$ galactocentric gradient

Adande & Ziurys (2012) evaluated the ^{14}N/^{15}N ratio across the galaxy through millimeter observations of CN and HNC in regions of star formation. They have enlarged the sample also with the high-mass sources observed by Dahmen et al. (1995) via HCN observations. In order to compare with their work we have plotted our ^{14}N/^{15}N ratios (for HCN and HNC together) as a function of the galactocentric distance of the sources (see Table C.1 and Fig. 5). We have computed a linear fit and we have obtained the relation:

$$^{14}\mathrm{N}/^{15}\mathrm{N} = (4.9 \pm 7.6)\ \mathrm{kpc}^{-1} \times D_{GC} + (366.5 \pm 65.6) \quad (2)$$

that is not in agreement with that obtained by Adande & Ziurys (2012):

$$^{14}\mathrm{N}/^{15}\mathrm{N} = (21.1 \pm 5.2)\ \mathrm{kpc}^{-1} \times D_{GC} + (123.8 \pm 37.1). \quad (3)$$

This indicates that in our dataset, the gradient found by Adande & Ziurys (2012) is not confirmed. We speculate that, as the beam used by Adande & Ziurys (2012) is larger, and hence more influenced by the diffuse surrounding material, the difference in ratios may be due to the material that is around the target cores, in which this ratio may be lower. We note also that Adande & Ziurys (2012) derived their fit using the source SgrB2(NW), located at a galactocentric radius of 0.1 kpc: for this source, they obtained a ^{14}N/^{15}N lower limit of 164. This value strongly influences their fit results, and hence could have a strong impact on both the slope and the intercept with the y-axis. Therefore, any comparison between the two fit results must be taken with caution.

5. Conclusions

We have observed the J=1-0 rotational transitions of H^{15}NC, HN^{13}C, H^{13}CN and HC^{15}N, together with J=2-1 transition of DNC, towards 27 massive star forming cores in different evolutionary stages, in order to derive the ^{15}N- and D-fractionation, and to compare each other. We find ^{14}N/^{15}N in HCN between ∼200 and ∼700, and in HNC between ∼260 and ∼600, with a small spread around the PSN value of 441. Comparing the ^{14}N/^{15}N ratios for different evolutionary stages we do not find any trend, indicating that time does not seem to play a role in the N-fractionation; furthermore we can not say anything about the correlation between the ^{15}N-fractionation for the two molecules, HNC and HCN. Considering both D- and ^{15}N-fractionation for HNC toward the same sources, we find no correlation. This is consistent with the lack of correlation found by Fontani et al. (2015a) in N_2H^+: the causes of D-enrichment in HCN and HNC do not affect the ^{15}N-fractionation. Our findings are in agreement with the recent chemical models of Roueff et al. (2015). The independence between D/H and ^{14}N/^{15}N ratios confirms the recent findings of Guzmán et al. (2017) in protoplanetary disks. Conversely, the low values of ^{14}N/^{15}N found by them (and the tentative decrease with decreasing distance to the star) is not in contrast with our findings, because our results are obtained on angular scales much larger than that of a protoplanetary disk. All this indicates that the ^{15}N enrichment is a local effect, which does not involve the larger-scale envelope.

Acknowledgments. We are grateful to the IRAM-30m telescope staff for their help during the observations. Many thanks to the anonymous Referee for the careful reading of the paper and his/her comments that improved the work. Paola Caselli and Luca Bizzocchi acknowledge support from the European Research Council (project PALs 320620).

References

Adams, F.C. 2010, ARA&A, 48, 74
Adande, G. R., & Ziurys, L. M. 2012, ApJ, 744, 194
Aléon, J., Engrand, C., Leshin, L. A., McKeegan, K., D. (2009). Geo. Cosmo. Acta. 73, 4558–4575.
Altwegg, K., Balsiger, H., Bar-Nun, A., et al. 2015, Sci, 347, 387
Banerjee et al. 2016, Nature Communications, 7, id. 13639
Bechtel, H., A. Steeves, and R. Field, ApJL 649, L53 (2006).
Bizzocchi, L., Caselli, P., Leonardo, E., & Dore, L. 2013, A&A, 555, AA109
Bonal, L., Huss, G.R., Nagashima, K., Krot, A.N.: *Meteoritics and Planetary Science Supplement*. 72, 5178(2009)
Busemann, H., A. F. Young, C. M. O. D. Alexander, P. Hoppe, S. Mukhopadhyay, and L. R. Nittler, Science 312(5774), 727–730 (2006).
Busquet, G., Estalella, R., Zhang, Q., et al. 2011, Astron. Astrophys., 525, A141
Caselli, P., & Ceccarelli, C. 2012, A&ARv, 20, 56
Caselli, P., Walmsley, C.M., Tafalla, M., Dore, L., Myers, P.C. 1999, ApJ, 523, L165
Caselli, P., Vastel, C., Ceccarelli, C., van der Tak, F.F.S., Crapsi, A., Bacmann, A. 2008, A&A, 492, 703
Caselli, P., Walmsley, C.M., Zucconi, A., et al. 2002a *ApJ*, 565, 344
Cazaux, S., Caselli, P., & Spaans, M. 2011, ApJ, 741, 34
Cazzoli, G., Puzzarini, C., & Gauss, J. 2005, ApJS, 159, 181
Cazzoli, G., Cludi, L., & Puzzarini, C. 2006, J. Mol. Struct., 780, 260
Ceccarelli C., Caselli P., Bockelee-Morvan D., Mousis O., Pizzarello S., Robert F., Semenov D., 2014, in Beuther H., Klessen R. S., Dullemond C. P., Henning T., eds, Protostars and Planets VI. University of Arizona Press, Tucson, p. 859
Codella, C., Fontani, F., Ceccarelli, C., Podio, L., Viti, S., Bachiller, R., Benedettini, M., Lefloch, B. 2015, MNRAS, 449, L11
Crapsi, A., Caselli, P., Walmsley, C.M., Myers, P.C., Tafalla, M., et al. 2005, ApJ, 619, 379
Dahmen, G.; Wilson, T. L.; Matteucci, F. 1995, A&A, 295, 194
Daniel F. et al., 2016, A&A, 592, A45
Emprechtinger M., Caselli P., Volgenau N. H., Stutzki J., Wiedner M. C., 2009, A&A , 493, 89
Fontani, F., Giannetti, A., Beltrán, M.T., Dodson, R., Rioja, M., Brand, J., Caselli, P., Cesaroni, R. 2012, MNRAS, 423, 2342
Fontani, F., Palau, Aina, Caselli, P., Sánchez-Monge, Á., Butler, M.J., et al. 2011, A&A, 529, L7
Fontani, F., Caselli, P., Palau, Aina, Bizzocchi, L, Ceccarelli, C. 2015a, ApJ, 808, L46
Fontani, F., Busquet, G., Palau, Aina, Caselli, P., Sánchez-Monge, Á., Tan, J.C., Audard, M. 2015b, 575, 87
Fontani, F. Sakai, Furuya, K., T., Sakai, N., Aikawa, Y., Yamamoto, S. 2014, MNRAS, 440, 448
Füri E., Marty B., 2015, Nat. Geosci., 8, 515
Geiss, J., Gloeckler, G.: *Abundances of Deuterium and Helium-3 in the Protosolar Cloud*. Space Science Reviews, 84, 239-250 (1998)
Gerin M, Marcelino N, Biver N, Roueff E, Coudert LH, et al. 2009. Astron. Astrophys. 498:L9–L12
Gerlich, D., Herbst, E., Roueff, E. 2002, P&SS, 50, 1275
Guzmán, V. V., Öberg, K. I., Huang, J., Loomis, R., Qi, C. 2017, ApJ, 836, article id. 30, 15 pp.
Hartogh, P., Lis, D. C., Bockelée-Morvan, D., et al. 2011, Natur, 478, 218
Heays A. N., Visser R., Gredel R., Ubachs W., Lewis B. R., Gibson S. T., van Dishoeck E. F., 2014, Astronomy & Astrophysics, 562, A61
Hily-Blant, P., Pineau des Forets, G., Faure, A., Le Gal, R., Padovani, M. 2013, A&A, 557, 65
Hily-Blant, P., Bonal, L., Faure, A., & Quirico, E. 2013, Icar, 223, 582
Hily-Blant, P., Magalhaes, V., Kastner, J., Faure, A., Forveille, T., Qi, C. 2017, A&A 603, L6
Hirota, T., Yamamoto, S., Mikami, H., & Ohishi, M. 1998, ApJ, 503, 717 Hunter, D. A. 2001, ApJ, 559, 225
Hoare, M.G., Kurtz, S.E., Lizano, S., Keto, E., Hofner, P. 2007, Protostars and Planets IV, pp 951
Jacobs A., Wahl M., Weller R., et al., 1989, Symp. Int. Combust. Proc., 22, 1093
Jin, M., Lee, J.-E., & Kim, K.-T. 2015, *ApJS*, 219, 2
Kong, S., Caselli, P., Tan, J.C., Wakelam, V., Sipilä, Olli 2015, ApJ, 804, 98
Kurtz S., Cesaroni R., Churchwell E., Hofner P., Walmsley C.M. 2000, Protostars and Planets IV, pp 299
Kutner, M.L., Ulich, B.L. 1981, *Ap.J.*, 250, 341
Linsky, J.L., Draine, B.T., Moos, H.W., Jenkins, E.B., Wood, B.E., et al. 2006, ApJ, 647, 1106
Lis DC, Phillips TG, Goldsmith PF, Neufeld DA, Herbst E, et al. 2010a. Astron. Astrophys. 521:L26
Loison J.-C., Wakelam V., Hickson K. M., 2014b, MNRAS, 443, 398
Manfroid, J., Jehin, E., Hutsemékers, D., et al.: *The CN isotopic ratios in comets*. A&A, 503, 613-624(2009)
Marty, B., Zimmermann, L., Burnard, P.G., Wieler, R., et al.: *Geochimica et Cosmochimica* Acta74, 340-355(2010)
Marty, B., Zimmermann, L., Burnard, P.G.: Geochimica et Cosmochimica Acta73, 842(2009)
Milam, S.N., Savage, C,m Brewster, M.A., Ziurys, L.M., Wyckoff, S. 2005, *Ap.J.*, 634, 1126
S.N. Milam, S.B. Charnley, Observations of nitrogen fractionation in prestellar cores: nitriles tracing interstellar chemistry. Technical report. Lunar and Planetary Institute Science Conference Abstracts vol. 43, p. 2618(2012)
Müller, H.S.P., Thorwirth, S., Roth, D. A., & Winnewisser, G. 2001, A&A, 370, L49
Müller, H.S.P, Schlüder, F., Stutzki, J., & Winnewisser, G. 2005, J. Mol. Struct., 42, 215
Owen, T., Mahaffy, P.R., Niemann, H.B., Atreya, S., Wong, M.:Protosolar Nitrogen. ApJL, 553, L77-L79
Pagani, L., Salez, M., & Wannier, P. G. 1992, A&A, 258, 479
Padovani, M., Walmsley, C. M., Tafalla, M., Hily-Blant, P., & Pineau Des Forêts, G. 2011, A&A, 534, A77
Pearson, E. F., Creswell, R. A., Winnewisser, M., & Winnewisser, G. 1976, ZNatA, 31a, 1394
Remusat, L., Robert, F., Meibom, A., et al., *ApJ*, 698, 2087-2092 (2009)
Robert, F. 2003. The D/H Ratio in Chondrites. Space Science Reviews 106, 87-101
Robert F. and Derenne S. (2006) Meteoritics and Planetary Science Supplement, 41, 5259.
Röllig, M., & Ossenkopf, V. 2013, A&A, **550**, A56
Roueff, E., Loison, J.C., Hickson, K.M. 2015, A&A, 576, 99
Schilke P., Walmsley C. M., Pineau Des Forets G., Roueff E., Flower D. R., Guilloteau S., 1992, A&A, 256, 595
Schoier F. L., Jørgensen J. K., van Dishoeck E. F., Blake G. A., 2002, A&A, 390, 1001
Shinnaka Y., Kawakita H., Jehin E., Decock A., Hutsemékers D., Manfroid J., Arai A., 2016, MNRAS, 462, p.S195-S209
Szűcs, László; Glover, Simon C. O.; Klessen, Ralf S., 2014, MNRAS, 445, 4055
Tafalla, M., Myers, P. C., Caselli, P., & Walmsley, C. M. 2004, A&A, 416, 191
Taquet, V., Ceccarelli, C., Kahane, C. 2012, A&A, 538, 42
Taquet, V., Peters, P.S., Kahane, C., Ceccarelli, C., López-Sepulcre, A. et al. 2013, A&A, 550, 127
Taquet, V., Furuya, K., Walsh, C., van Dishoeck, E.F. 2016, MNRAS, 462, 99
Terzieva R., Herbst E., 2000, MNRAS, 317, 563
van der Tak, F. F. S., Müller, H. S. P., Harding, M. E., & Gauss, J. 2009, A&A, 507, 347
Walmsley C. M., Flower D. R., Pineau des Forêts G., 2004, A&A, 418, 1035
Wampfler, S. F., Jørgensen, J. K., Bizzarro, M., & Bisschop, S. E. 2014, A&A, 572, A24
Wirström, E.S., Charnley, S.B., Cordiner, M.A., Milam, S.N. 2012, 757, L11
Zeng, S., Jimenez-Serra, I., Cosentino, G., Viti, S., Barnes, A. T., Henshaw, J. D., Caselli, P., Fontani, F., Hily-Blant, P., 2017, arXiv:1705.04082

Table 3. Total column densities (beam-averaged), computed as explained in Sect. 3, of $H^{15}NC$, $HN^{13}C$ and DNC. In the third and fifth columns there are the error on column densities without considering the calibration error (ΔN). In the seventh, eighth and ninth columns there are the corresponding $^{14}N/^{15}N$ and D/H isotopic ratios. Uncertainties in the column densities and in the isotope ratios have been computed as explained in Sect. 3.1 and 3.2. In the last column there are the kinetic temperatures of the clumps derived from Fontani et al. (2015a): for the sources without a derivation of T_k, the mean value for that evolutionary stage was taken (for the HMSCs the average was done without the "warm" ones, i.e those with a $T_k < 20$ K).

Source	N($H^{15}NC$) ($\times10^{10}$cm^{-2})	ΔN	N($HN^{13}C$) ($\times10^{11}$cm^{-2})	ΔN	N(DNC) (10^{11}cm^{-2})	$\frac{HNC}{H^{15}NC}$ *	$\frac{HNC}{DNC}$ **	$\frac{DNC}{HNC}$	T_k (K)
					HMSC				
I00117-MM2	12 ± 4	2	8 ± 1	0.4	4.2 ± 0.6	460 ± 80	406 ± 77	$(2.5 \pm 0.5) \times 10^{-3}$	14
AFGL5142-EC^{w}	104 ± 20	10	56 ± 7	1	19 ± 3	398 ± 39	674 ± 136	$(1.5 \pm 0.3) \times 10^{-3}$	25
05358-mm3^{w}	141 ± 24	10	74 ± 9	1	27 ± 3	388 ± 28	627 ± 103	$(1.6 \pm 0.3) \times 10^{-3}$	30
G034-G2(MM2)	26 ± 8	5	19 ± 3	0.6	4.8 ± 0.7	365 ± 71	612 ± 131	$(1.6 \pm 0.3) \times 10^{-3}$	16*
G034-F1(MM8)	19 ± 4	2	20 ± 4	2	2.9 ± 0.4	495 ± 72	1002 ± 243	$(1.0 \pm 0.2) \times 10^{-3}$	16*
G034-F2(MM7)	6 ± 3	2	10 ± 1	0.4	1.6 ± 0.3	783 ± 263	908 ± 193	$(1.1 \pm 0.2) \times 10^{-3}$	16*
G028-C1(MM9)	43 ± 8	4	28 ± 6	2	3.2 ± 0.8	260 ± 30	1081 ± 356	$(0.9 \pm 0.3) \times 10^{-3}$	17
G028-C3(MM11)	13 ± 4	2	11 ± 1	0.4	1.0 ± 0.3	338 ± 53	1360 ± 426	$(0.7 \pm 0.2) \times 10^{-3}$	17
I20293-WC	24 ± 7	4	17 ± 4	2	10 ± 1	439 ± 90	326 ± 83	$(3.1 \pm 0.8) \times 10^{-3}$	17
I22134-G^{w}	43 ± 8	4	23 ± 3	0.5	4.4 ± 0.6	369 ± 35	1114 ± 210	$(0.9 \pm 0.2) \times 10^{-3}$	25
I22134-B	10 ± 3	2	6.0 ± 0.9	0.3	1.3 ± 0.2	414 ± 85	984 ± 211	$(1.0 \pm 0.2) \times 10^{-3}$	17
					HMPO				
I00117-MM1	16 ± 4	3	9 ± 1	0.4	3.0 ± 0.5	388 ± 75	640 ± 128	$(1.6 \pm 0.3) \times 10^{-3}$	20
AFGL5142-MM	147 ± 24	9	86 ± 10	1	39 ± 5	433 ± 27	504 ± 87	$(2.0 \pm 0.3) \times 10^{-3}$	34
05358-mm1	154 ± 25	9	97 ± 11	2	25 ± 3	466 ± 29	887 ± 146	$(1.1 \pm 0.2) \times 10^{-3}$	39
18089-1732	58 ± 34	29	52 ± 14	9	12 ± 2	385 ± 204	576 ± 182	$(1.7 \pm 0.5) \times 10^{-3}$	38
18517+0437	130 ± 21	8	89 ± 10	1	25 ± 3	349 ± 21	561 ± 92	$(1.8 \pm 0.3) \times 10^{-3}$	40*
G75-core	124 ± 31	18	109 ± 16	5	10 ± 1	554 ± 84	2122 ± 377	$(5.0 \pm 0.9) \times 10^{-4}$	96
I20293-MM1	103 ± 17	7	80 ± 9	1	12 ± 2	481 ± 33	1277 ± 257	$(0.8 \pm 0.1) \times 10^{-3}$	36
I21307	$\leq 15^{u}$	–	7 ± 1	0.6	2.1 ± 0.4	≥ 317	700 ± 167	$(1.4 \pm 0.4) \times 10^{-3}$	21
I23385	19 ± 7	5	15 ± 3	2	2.4 ± 0.6	639 ± 189	1564 ± 501	$(0.6 \pm 0.2) \times 10^{-3}$	37
					UC HII				
G5.89-0.39	576 ± 70	13	453 ± 49	3	33 ± 4	432 ± 10	2333 ± 379	$(4.3 \pm 0.7) \times 10^{-4}$	32*
I19035-VLA1	54 ± 16	10	57 ± 7	2	6 ± 1	570 ± 107	1585 ± 328	$(0.6 \pm 0.1) \times 10^{-3}$	39
19410+2336	74 ± 11	4	55 ± 6	0.6	15 ± 2	431 ± 24	657 ± 113	$(1.5 \pm 0.3) \times 10^{-3}$	21
ON1	149 ± 21	6	116 ± 12	0.9	22 ± 2	467 ± 19	978 ± 135	$(1.0 \pm 0.1) \times 10^{-3}$	26
I22134-VLA1	53 ± 11	6	28 ± 4	0.9	6.3 ± 0.9	364 ± 43	948 ± 191	$(1.1 \pm 0.2) \times 10^{-3}$	47
23033+5951	82 ± 15	7	44 ± 5	0.9	8.1 ± 0.9	397 ± 35	1242 ± 197	$(0.8 \pm 0.1) \times 10^{-3}$	25
NGC 7538-IRS9	100 ± 21	11	46 ± 6	1	9 ± 1	331 ± 37	1137 ± 195	$(0.9 \pm 0.1) \times 10^{-3}$	32*

* it has been multiplied by $\frac{^{12}C}{^{13}C}$ as described in Section (3.1) and given in Table C.1;

** it has been multiplied by $\frac{^{12}C}{^{13}C}$ and by the correction of the different beams 3.09;

^{t} tentative detection;

^{u} upper limits;

^{w}: "warm" HMSC;

* average value for the specific evolutionary stage.

Table 4. Total column densities (beam-averaged), computed as explained in Sect. (3), of $HC^{15}N$ and $H^{13}CN$(1-0) transitions. In the third and fifth columns there are the error on column densities without considering the calibration error (ΔN). In the sixth column there is the corresponding $^{14}N/^{15}N$ isotopic ratios. Uncertainties have been derived as explained in the caption of Table 3. In the last column there are the kinetic temperatures of the clumps derived from Fontani et al. (2015a).

Source	N($HC^{15}N$) ($\times10^{10}$cm^{-2})	ΔN	N($H^{13}CN$) ($\times10^{11}$cm^{-2})	ΔN	$\frac{HCN}{HC^{15}N}$ *	T_k (K)
			HMSC			
I00117-MM2	22 ± 6	4	9 ± 1	0.5	282 ± 54	14
AFGL5142-EC^{w}	327 ± 47	14	176 ± 20	2	398 ± 18	25
05358-mm3^{w}	270 ± 39	12	158 ± 18	2	433 ± 20	30
G034-G2(MM2)	≤ 17^{u}	–	5 ± 1	0.3	≥ 147	16*
G034-F1(MM8)	14 ± 4	3	11 ± 2	0.4	369 ± 80	16*
G034-F2(MM7)	≤ 14^{u}	–	5 ± 1	0.3	≥ 168	16*
G028-C1(MM9)	32 ± 9^{t}	6	23 ± 3	0.7	287 ± 55	17
G028-C3(MM11)	≤ 16^{u}	–	10 ± 2	0.8	≥ 250	17
I20293-WC	31 ± 12	9	31 ± 4	0.6	620 ± 180	17
I22134-G^{w}	120 ± 17	5	56 ± 6	0.8	322 ± 14	25
I22134-B	17 ± 4	2	10 ± 1	0.4	406 ± 50	17
			HMPO			
I00117-MM1	38 ± 8	4	19 ± 2	0.6	345 ± 38	20
AFGL5142-MM	558 ± 70	14	292 ± 31	2	387 ± 10	34
05358-mm1	351 ± 50	14	205 ± 23	2	432 ± 18	39
18089-1732	354 ± 36	9	278 ± 30	2	338 ± 9	38
18517+0437	405 ± 52	11	259 ± 28	2	326 ± 9	40*
G75-core	790 ± 88	9	324 ± 35	2	258 ± 3	96
I20293-MM1	187 ± 28	9	152 ± 17	2	504 ± 25	36
I21307	35 ± 7	4	20 ± 3	0.7	389 ± 46	21
I23385	134 ± 26	12	48 ± 6	0.9	290 ± 26	37
			UC HII			
G5.89-0.39	1674 ± 246	81	775 ± 79	2	255 ± 12	32*
I19035-VLA1	157 ± 28	12	99 ± 11	2	340 ± 27	39
19410+2336	176 ± 23	5	123 ± 13	1	405 ± 12	21
ON1	319 ± 40	8	174 ± 18	1	327 ± 8	26
I22134-VLA1	152 ± 22	7	86 ± 10	1	390 ± 18	47
23033+5951	155 ± 23	7	96 ± 11	1	458 ± 21	25
NGC 7538-IRS9	288 ± 43	14	164 ± 18	1	410 ± 20	32*

* it has been multiplied by $\frac{^{12}C}{^{13}C}$ as described in Section (3.1) and given in Table C.1;
^{t} tentative detection;
^{u} upper limits;
^{w}: "warm" HMSC;
* average value for the specific evolutionary stage.

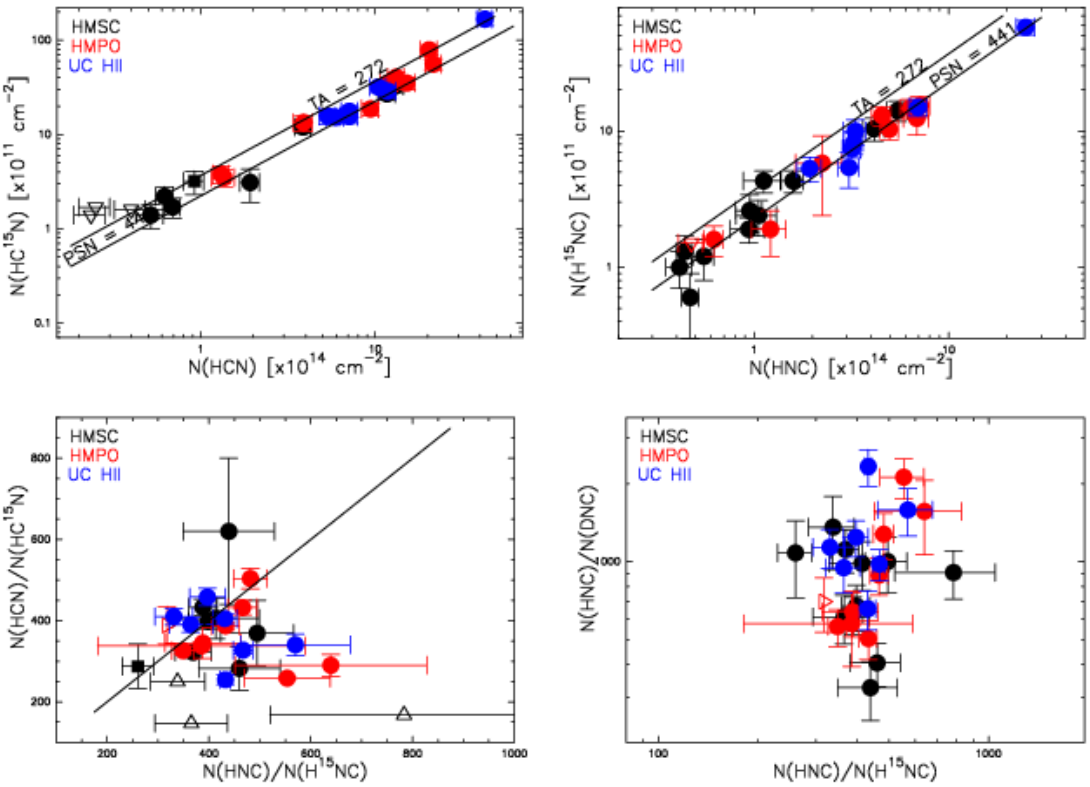

Fig. 1. Top panels: column density of HCN against that of $HC^{15}N$ (left) and of HNC against that of $H^{15}NC$ (right). Bottom panels: comparison between the $^{14}N/^{15}N$ isotopic ratios derived from the column density ratios N(HCN)/N($HC^{15}N$) and N(HNC)/N($H^{15}NC$) (right) and comparison between the H/D and $^{14}N/^{15}N$ isotopic ratios in HNC (left). In all panels, the filled circles represent the detected sources (black=HMSCs; red=HMPOs; blue=UC HIIs). The open triangles in the top panels are the upper limits on N($H^{15}NC$) (left) and N($HC^{15}N$) (right), while in the bottom panels the open triangles indicate lower limits on either N(HCN)/N($HC^{15}N$) or N(HNC)/N($H^{15}NC$). The filled squares represent tentative detections. The solid lines in the top panels indicate the mean atomic composition as measured in the terrestrial atmosphere (TA) and in the protosolar nebula (PSN), while in the bottom-left panel the solid line indicate the locus of points where N(HCN)/N($HC^{15}N$) is equal to N(HNC)/N($H^{15}NC$).

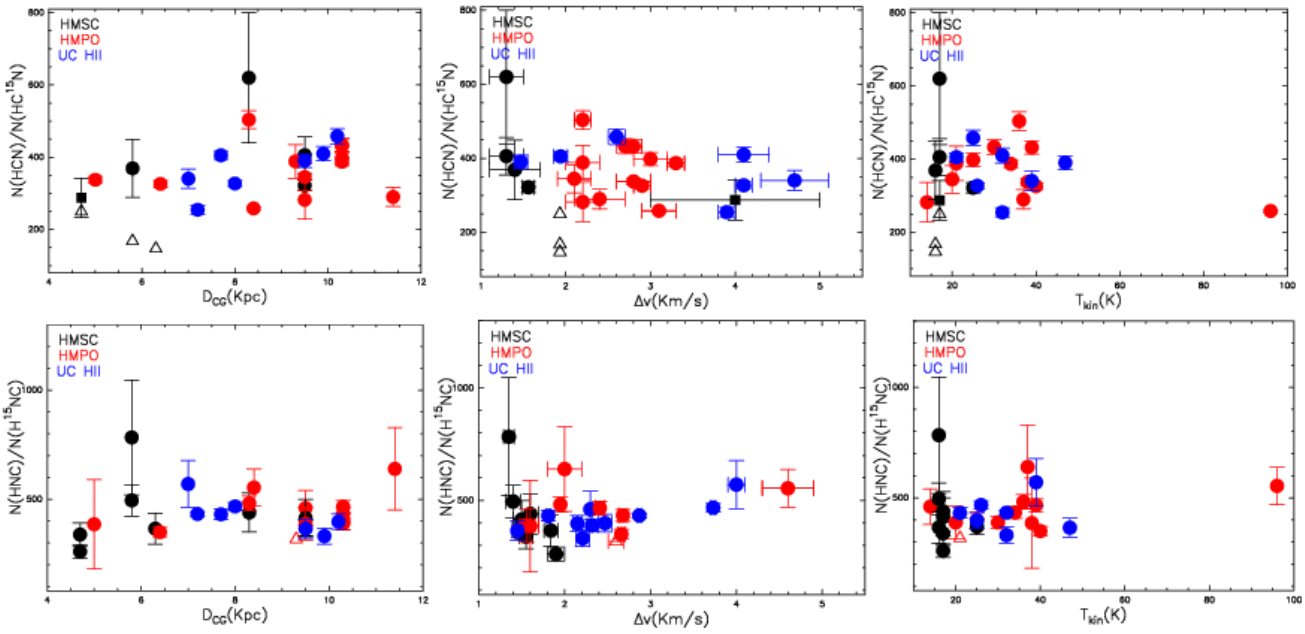

Fig. 2. Top panels: N(HCN)/N(HC^{15}N) as a function of Galactocentric distances, line widhts and kinetic temperatures. Bottom panels: N(HNC)/N(H^{15}NC) as a function of Galactocentric distances, line widhts and kinetic temperatures. The symbolism is the same used for bottom panels of Fig.1.

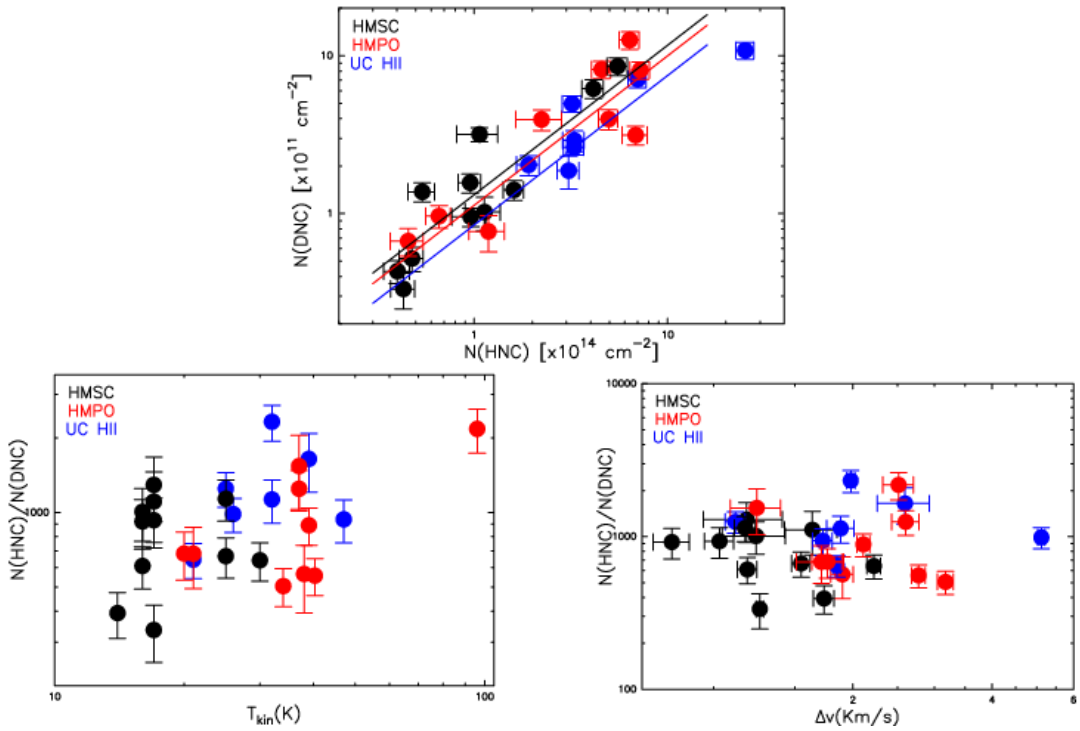

Fig. 3. Top panel: column density of HNC against that of DNC. The three lines represent the mean values of D/H (see text) for different evolutionary stages: in black for HMSCs, in red for HMPOs and in blue for UC HIIs. Bottom panels: N(HNC)/N(DNC) as a function of line widths and kinetic temperatures. The symbolism of filled circles is the same used for Fig.1.

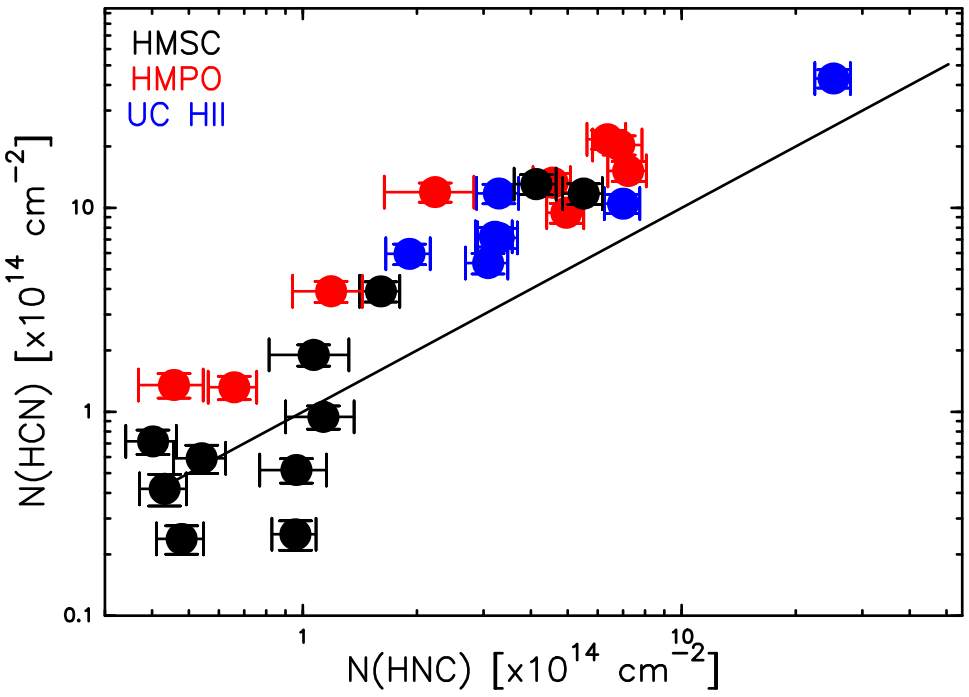

Fig. 4. Column density of HCN against that of HNC. The solid line is the locus where N(HCN)/N(HNC) is equal to 1 as statistically expected. The symbolism of filled circles is the same used for Fig.1.

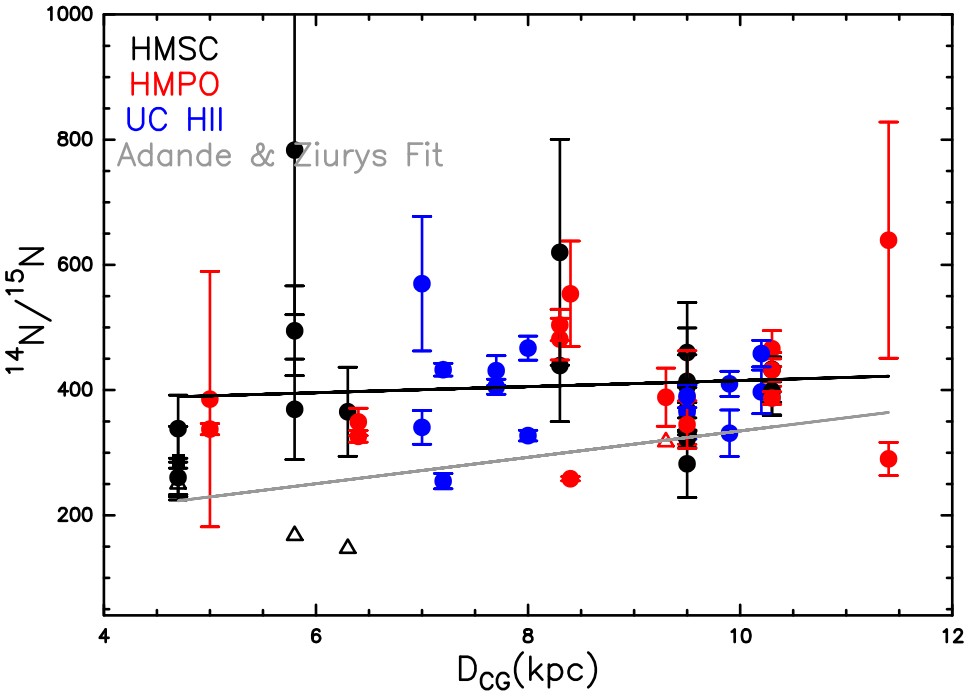

Fig. 5. $^{14}N/^{15}N$ ratios as a function of Galactocentric distances (for HNC and HCN together). The symbolism is the same used for bottom panels of Fig.1. The black line is the linear fit computed for the plotted data and the grey line is the Adande & Ziurys (2012) fit.

Appendix A: Fit results

In this appendix, the results of the fitting procedure to the $HN^{13}C$(1-0), $H^{15}NC$(1-0), $HC^{15}N$(1-0), DNC(2-1) and $H^{13}CN$(1-0) lines of all sources (see Sect. 3.1 and 3.2) are shown.

Table A.1. Values obtained with a Gaussian fit to the $HN^{13}C$ and $H^{15}NC$(1-0) lines. The errors are coming from the fitting procedure and are not taking account the calibration error on T_{MB}. In the second and in the third columns the centroid velocities and the FWHM are listed. In the fourth column there are the integrated intensities and in the fifth column there is the r.m.s of the **spectra**. The cases in which the line is not detected, and therefore only column density upper limits could be obtained as explained in Sect. 3.1, are indicated with – . The source names are taken from Fontani et al. (2015b).

Source	$HN^{13}C$(1-0)				$H^{15}NC$(1-0)			
	v_{LSR} (km/s)	$\Delta v_{1/2}$ (km/s)	$\int T_{MB}\,dv$ (K km/s)	σ (mK)	v_{LSR} (km/s)	$\Delta v_{1/2}$ (km/s)	$\int T_{MB}\,dv$ (K km/s)	σ (mK)
HMSC								
I00117-MM2	−35.27 ± 0.06	2.30 ± 0.02	0.30 ± 0.02	10	−35.1 ± 0.1	1.3 ± 0.4	0.05 ± 0.01	9
AFGL5142-EC	−1.92 ± 0.03	2.47 ± 0.08	1.43 ± 0.04	30	−1.60 ± 0.08	1.9 ± 0.2	0.28 ± 0.03	20
05358-mm3	−15.39 ± 0.02	2.32 ± 0.06	1.65 ± 0.03	20	−14.92 ± 0.08	2.2 ± 0.2	0.32 ± 0.02	20
G034-G2(MM2)	42.24 ± 0.03	1.84 ± 0.08	0.67 ± 0.02	20	42.9 ± 0.2	2.4 ± 0.6	0.1 ± 0.02	10
G034-F1(MM8)	58.74 ± 0.06	1.40 ± 0.09	0.72 ± 0.07	10	59.20 ± 0.09	1.4 ± 0.2	0.07 ± 0.01	10
G034-F2(MM7)	56.93 ± 0.03	1.35 ± 0.06	0.36 ± 0.01	10	57.3 ± 0.1	0.7 ± 0.2	0.02 ± 0.008	7
G028-C1(MM9)	81.19 ± 0.09	1.9 ± 0.1	0.95 ± 0.1	10	80.9 ± 0.1	2.7 ± 0.3	0.15 ± 0.01	9
G028-C3(MM11)	81.56 ± 0.03	1.55 ± 0.08	0.36 ± 0.01	10	82.1 ± 0.2	1.6 ± 0.3	0.05 ± 0.009	8
I20293-WC	7.76 ± 0.09	1.6 ± 0.1	0.58 ± 0.08	10	8.4 ± 0.1	1.2 ± 0.2	0.09 ± 0.01	10
I22134-G	−17.85 ± 0.01	1.47 ± 0.04	0.60 ± 0.01	10	−17.55 ± 0.06	1.5 ± 0.2	0.11 ± 0.01	10
I22134-B	−17.98 ± 0.04	1.5 ± 0.1	0.20 ± 0.01	10	−17.43 ± 0.09	1.0 ± 0.2	0.03 ± 0.006	7
HMPO								
I00117-MM1	−35.44 ± 0.04	1.56 ± 0.09	0.29 ± 0.01	10	−35.1 ± 0.1	1.2 ± 0.2	0.05 ± 0.008	9
AFGL5142-MM	−2.01 ± 0.02	2.68 ± 0.05	1.72 ± 0.03	20	−1.70 ± 0.07	2.2 ± 0.1	0.30 ± 0.02	10
05358-mm1	−15.53 ± 0.02	2.41 ± 0.05	1.73 ± 0.03	20	−15.23 ± 0.06	2.0 ± 0.1	0.28 ± 0.02	10
18089-1732	32.30 ± 0.03	1.6 ± 0.1	0.9 ± 0.2	20	32.7 ± 0.2	1.4 ± 0.3	0.11 ± 0.05	10
18517+0437	44.52 ± 0.02	2.66 ± 0.04	1.54 ± 0.02	10	44.84 ± 0.08	2.5 ± 0.2	0.23 ± 0.01	10
G75-core	0.57 ± 0.07	4.6 ± 0.3	0.86 ± 0.04	10	1.1 ± 0.1	1.9 ± 0.4	0.10 ± 0.01	10
I20293-MM1	6.67 ± 0.01	1.95 ± 0.03	1.49 ± 0.02	10	7.02 ± 0.06	1.8 ± 0.1	0.20 ± 0.01	10
I21307	−45.8 ± 0.01	2.6 ± 0.3	0.20 ± 0.02	10	–	–	–	8
I23385	−49.5 ± 0.1	2.0 ± 0.2	0.27 ± 0.03	10	−49.1 ± 0.2	1.4 ± 0.5	0.04 ± 0.009	9
UC H_{II}								
G5.89-0.39	9.05 ± 0.01	2.87 ± 0.02	9.54 ± 0.07	30	9.35 ± 0.03	2.93 ± 0.08	1.26 ± 0.03	10
I19035-VLA1	33.33 ± 0.05	4.0 ± 0.1	1.01 ± 0.03	20	33.1 ± 0.2	2.6 ± 0.8	0.1 ± 0.02	10
19410+2336	23.16 ± 0.01	1.81 ± 0.03	1.60 ± 0.02	20	23.50 ± 0.03	1.45 ± 0.09	0.22 ± 0.01	10
ON1	12.25 ± 0.01	3.73 ± 0.03	2.89 ± 0.02	10	12.70 ± 0.06	3.3 ± 0.2	0.38 ± 0.02	10
I22134-VLA1	−17.83 ± 0.02	1.45 ± 0.06	0.45 ± 0.01	10	−17.48 ± 0.08	1.5 ± 0.2	0.08 ± 0.009	8
23033+5951	−52.54 ± 0.02	2.15 ± 0.05	0.14 ± 0.02	20	−52.27 ± 0.09	2.2 ± 0.2	0.22 ± 0.02	10
NGC 7538-IRS9	−56.37 ± 0.03	2.21 ± 0.08	0.97 ± 0.03	20	−56.1 ± 0.1	3.0 ± 0.5	0.22 ± 0.02	10

Table A.2. Values obtained with Gaussian fits to the $HC^{15}N$ and DNC(2-1) lines. The errors are coming from the fitting procedure and do not take the calibration error on T_{MB} into account. In the second and in the third colums are listed the centroid velocities and the line FWHM, respectively. In the fourth column there are the integrated intensities and in the fifth column there is the r.m.s of the spectra. The cases in which the line is not detected, and therefore only column density upper limits could be obtained as explained in Sect. 3.1, are indicated with – .

Source	$HC^{15}N$(1-0)				DNC(2-1)			
	v_{LSR} (km/s)	$\Delta v_{1/2}$ (km/s)	$\int T_{MB}\,dv$ (K km/s)	σ (mK)	v_{LSR} (km/s)	$\Delta v_{1/2}$ (km/s)	$\int T_{MB}\,dv$ (K km/s)	σ (mK)
HMSC								
I00117-MM2	−35.8 ± 0.2	2.2 ± 0.4	0.11 ± 0.02	10	−34.83 ± 0.03	1.73 ± 0.09	0.41 ± 0.02	20
AFGL5142-EC	−2.64 ± 0.07	3.0 ± 0.2	1.07 ± 0.05	30	−1.67 ± 0.03	1.55 ± 0.07	1.50 ± 0.05	60
05358-mm3	−16.01 ± 0.06	2.7 ± 0.1	0.76 ± 0.03	20	−15.38 ± 0.03	2.22 ± 0.08	1.88 ± 0.05	50
G034-G2(MM2)	–	–	–	10	42.18 ± 0.02	1.18 ± 0.06	0.46 ± 0.02	20
G034-F1(MM8)	58.0 ± 0.2	1.4 ± 0.3	0.06 ± 0.01	10	58.5 ± 0.2	1.2 ± 0.2	0.27 ± 0.01	20
G034-F2(MM7)	–	–	–	10	56.74 ± 0.03	0.81 ± 0.07	0.15 ± 0.01	20
*G028-C1(MM9)	80.3 ± 0.4	4 ± 1	0.14 ± 0.03	10	81.4 ± 0.1	1.6 ± 0.2	0.29 ± 0.04	20
G028-C3(MM11)	–	–	–	10	81.32 ± 0.09	1.2 ± 0.2	0.1 ± 0.01	20
I20293-WC	7.5 ± 0.1	1.3 ± 0.2	0.13 ± 0.04	10	7.80 ± 0.01	1.26 ± 0.02	0.91 ± 0.03	20
I22134-G	−18.46 ± 0.03	1.56 ± 0.07	0.39 ± 0.01	10	−18.13 ± 0.02	1.17 ± 0.06	0.34 ± 0.02	20
I22134-B	−18.25 ± 0.08	1.3 ± 0.2	0.07 ± 0.008	9	−18.37 ± 0.04	1.03 ± 0.07	0.12 ± 0.08	10
HMPO								
I00117-MM1	−36.0 ± 0.1	2.1 ± 0.2	0.15 ± 0.06	10	−35.48 ± 0.05	1.8 ± 0.1	0.26 ± 0.02	20
AFGL5142-MM	−2.67 ± 0.04	3.3 ± 0.1	1.42 ± 0.04	20	−1.62 ± 0.04	3.2 ± 0.1	2.55 ± 0.08	60
05358-mm1	−16.12 ± 0.05	2.8 ± 0.1	0.80 ± 0.03	20	−15.62 ± 0.03	2.11 ± 0.07	1.50 ± 0.04	40
18089-1732	32.15 ± 0.07	2.8 ± 0.2	0.820 ± 0.002	20	32.19 ± 0.05	1.9 ± 0.1	0.74 ± 0.04	30
18517+0437	44.00 ± 0.04	2.9 ± 0.1	0.89 ± 0.03	20	44.37 ± 0.04	2.77 ± 0.09	1.48 ± 0.04	40
G75-core	0.07 ± 0.01	3.1 ± 0.2	0.79 ± 0.09	10	0.3 ± 0.2	2.5 ± 0.2	0.28 ± 0.01	20
I20293-MM1	6.42 ± 0.05	2.2 ± 0.1	0.44 ± 0.02	20	6.53 ± 0.06	2.6 ± 0.2	0.76 ± 0.04	30
I21307	−46.2 ± 0.1	2.2 ± 0.2	0.13 ± 0.01	10	−46.29 ± 0.08	1.7 ± 0.2	0.18 ± 0.02	20
I23385	−50.1 ± 0.01	2.4 ± 0.3	0.32 ± 0.03	10	−49.43 ± 0.07	1.2 ± 0.2	0.15 ± 0.02	20
UC H_{II}								
G5.89-0.39	8.94 ± 0.03	3.9 ± 0.1	4.4 ± 0.2	20	8.06 ± 0.01	1.98 ± 0.04	2.28 ± 0.06	30
I19035-VLA1	32.9 ± 0.2	4.7 ± 0.4	0.35 ± 0.03	10	32.9 ± 0.1	2.6 ± 0.3	0.34 ± 0.05	20
19410+2336	22.60 ± 0.03	1.94 ± 0.08	0.66 ± 0.02	20	22.87 ± 0.01	1.85 ± 0.04	1.31 ± 0.02	20
ON1	11.83 ± 0.05	4.1 ± 0.1	1.01 ± 0.03	10	12.59 ± 0.04	5.11 ± 0.09	1.69 ± 0.03	20
I22134-VLA1	−18.34 ± 0.03	1.47 ± 0.08	0.09 ± 0.001	10	−18.19 ± 0.04	1.72 ± 0.08	0.33 ± 0.01	20
23033+5951	−52.93 ± 0.06	2.6 ± 0.1	0.51 ± 0.02	20	−52.48 ± 0.02	1.11 ± 0.06	0.64 ± 0.004	30
NGC 7538-IRS9	−56.82 ± 0.08	4.1 ± 0.3	0.77 ± 0.04	20	−56.54 ± 0.05	1.9 ± 0.1	0.61 ± 0.03	30

* tentative detection, as explained in Sect. 3.1.

Table A.3. Values obtained from the hyperfine fit of the $H^{13}CN$(1-0) lines. The errors are coming from the fitting procedure and are not taking into account of the calibration error on T_{MB}. In the second and in the third colums are listed the centroid velocities and the FWHM, respectively. In the fourth and fifth columns there are the optical depths and the antenna temperatures times the optical depths. In the sixth column are listed the r.m.s of the spectra, and finally in the last column there are the integrated intensities that, in this case, are not obtained from the fitting procedure but from the PRINT AREA command in CLASS.

Source	v_{LSR} (km/s)	$\Delta v_{1/2}$ (km/s)	τ	$T_A \times \tau$ (K)	σ (mK)	$\int T_{MB}\, dv$ (K km/s)
			HMSC			
I00117-MM2	−36.37 ± 0.05	1.8 ± 0.1	0.1 ± 0.1	0.142 ± 0.008	10	0.42 ± 0.02
AFGL5142-EC	−3.35 ± 0.02	3.30 ± 0.04	0.10 ± 0.06	0.94 ± 0.01	30	5.81 ± 0.08
05358-mm3	−16.65 ± 0.03	3.00 ± 0.05	0.10 ± 0.04	0.80 ± 0.01	30	4.51 ± 0.07
G034-G2(MM2)	41.1 ± 0.1	1.7 ± 0.2	0.1 ± 0.4	0.087 ± 0.007	10	0.23 ± 0.02
G034-F1(MM8)	57.62 ± 0.08	1.7 ± 0.1	0.1 ± 0.4	0.16 ± 0.01	10	0.50 ± 0.02
G034-F2(MM7)	55.69 ± 0.04	0.8 ± 0.1	0.25 ± 0.02	0.11 ± 0.01	10	0.23 ± 0.01
G028-C1(MM9)	79.43 ± 0.05	3.09 ± 0.09	0.1 ± 0.2	0.180 ± 0.006	10	1.02 ± 0.03
G028-C3(MM11)	80.31 ± 0.08	2.2 ± 0.3	0.5 ± 0.7	0.12 ± 0.03	10	0.45 ± 0.03
I20293-WC	6.83 ± 0.06	1.0 ± 0.1	0.60 ± 0.03	0.15 ± 0.02	10	1.33 ± 0.03
I22134-G	−19.04 ± 0.01	1.65 ± 0.03	0.10 ± 0.03	0.63 ± 0.01	10	1.85 ± 0.03
I22134-B	−18.95 ± 0.02	1.43 ± 0.06	0.1 ± 0.4	0.164 ± 0.006	10	0.45 ± 0.02
			HMPO			
I00117-MM1	−36.54 ± 0.03	1.96 ± 0.09	0.3 ± 0.3	0.21 ± 0.02	10	0.74 ± 0.02
AFGL5142-MM	−3.43 ± 0.01	3.27 ± 0.03	0.26 ± 0.06	1.27 ± 0.03	20	7.52 ± 0.05
05358-mm1	−16.8 ± 0.02	2.99 ± 0.04	0.50 ± 0.02	0.91 ± 0.01	20	4.68 ± 0.06
18089-1732	31.8 ± 0.4	2 ± 1	0.1 ± 0.1	01.48 ± 0.02	30	6.51 ± 0.05
18517+0437	43.29 ± 0.01	2.97 ± 0.02	0.1 ± 0.03	1.024 ± 0.007	20	5.76 ± 0.05
G75-core	−0.596 ± 0.004	2.5 ± 0.1	0.1 ± 0.02	0.48 ± 0.02	10	3.27 ± 0.02
I20293-MM1	5.79 ± 0.02	2.38 ± 0.03	0.100 ± 0.002	0.80 ± 0.01	20	3.64 ± 0.04
I21307	−47.00 ± 0.04	2.3 ± 0.1	0.2 ± 0.3	0.18 ± 0.02	10	0.75 ± 0.03
I23385	−50.9 ± 0.3	1 ± 1	0.6 ± 0.1	0.26 ± 0.01	10	1.16 ± 0.02
			UC H_{II}			
G5.89-0.39	8.24 ± 0.01	3.83 ± 0.01	0.12 ± 0.01	3.75 ± 0.2	30	20.97 ± 0.05
I19035-VLA1	32.17 ± 0.05	4.4 ± 0.1	0.4 ± 0.2	0.30 ± 0.02	10	2.26 ± 0.04
19410+2336	22.01 ± 0.002	2.186 ± 0.002	0.10 ± 0.02	1.090 ± 0.005	20	4.64 ± 0.04
ON1	11.12 ± 0.02	3.71 ± 0.04	0.73 ± 0.08	0.93 ± 0.03	10	5.55 ± 0.04
I22134-VLA1	−18.98 ± 0.01	1.76 ± 0.03	0.10 ± 0.03	0.513 ± 0.007	10	1.67 ± 0.03
23033+5951	−53.63 ± 0.02	2.73 ± 0.02	0.10 ± 0.02	0.621 ± 0.003	20	3.17 ± 0.04
NGC 7538-IRS9	−57.64 ± 0.02	3.60 ± 0.04	0.10 ± 0.03	0.65 ± 0.01	20	4.43 ± 0.04

Appendix B: Spectra

In this appendix, all spectra of $HN^{13}C$(1-0), $H^{13}CN$(1-0), $H^{15}NC$(1-0), $HC^{15}NC$(1-0) and DNC(2-1) transitions for all the sources are shown.

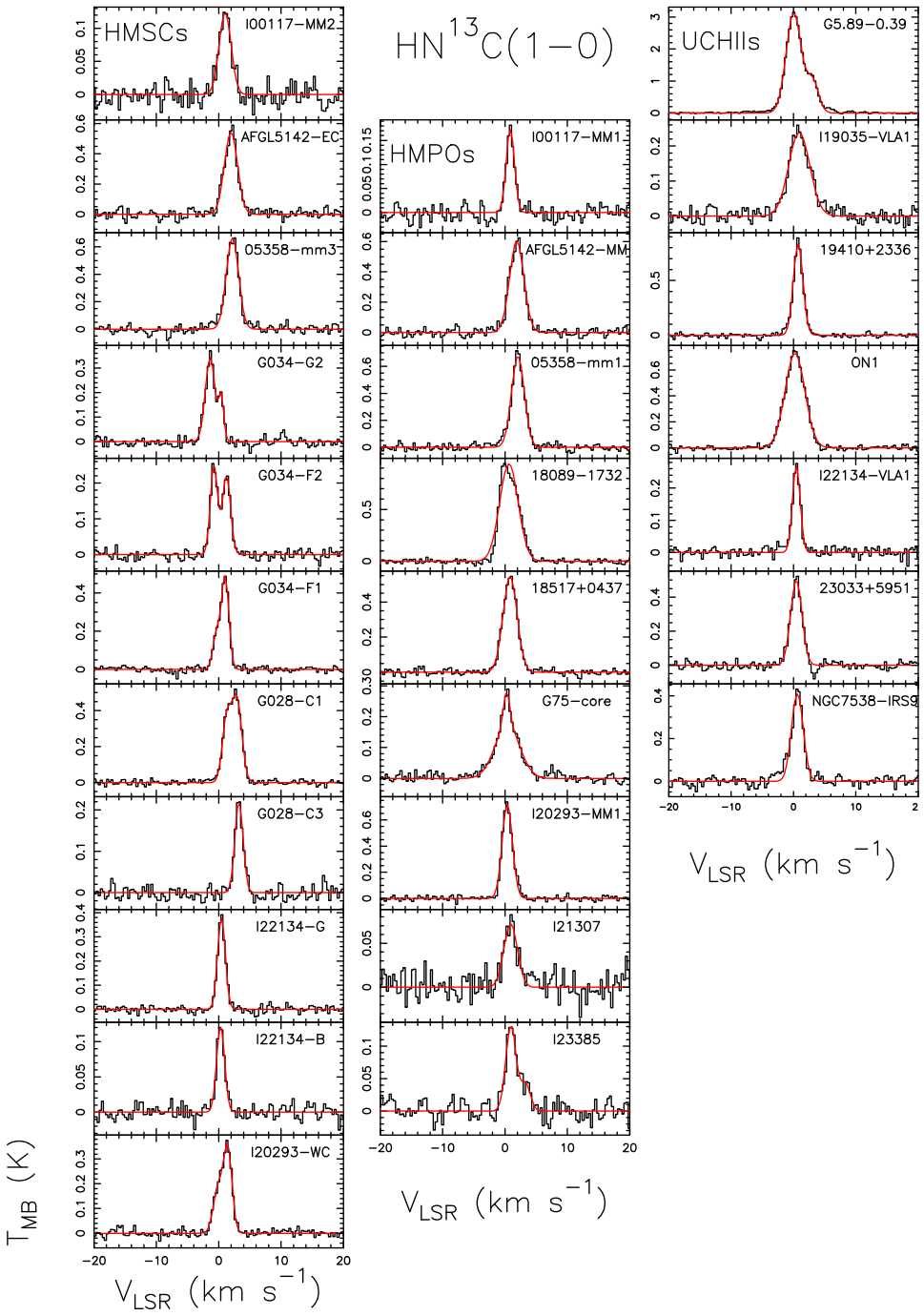

Fig. B.1. Spectra of $HN^{13}C$(1-0) obtained for the sources classified as HMSCs (first column), HMPOs (second column) and UC HII regions (third column) . For each spectrum the x-axis represents a velocity interval of ±20 km s^{-1} around the systemic velocity listed in Tab. 1 of Fontani et al. (2015b). The y-axis shows the intensity in main beam temperature units. The red curves are the best Gaussian fits obtained with CLASS. Note that for some sources (I20293-WC, G034-G2, G034-F2, G5.89-0.39, G034-F1, G028-C1 and I23385) we have observed two components: we have fitted both lines, and we have used only the one centered on the systemic velocity of the source to compute the column densities.

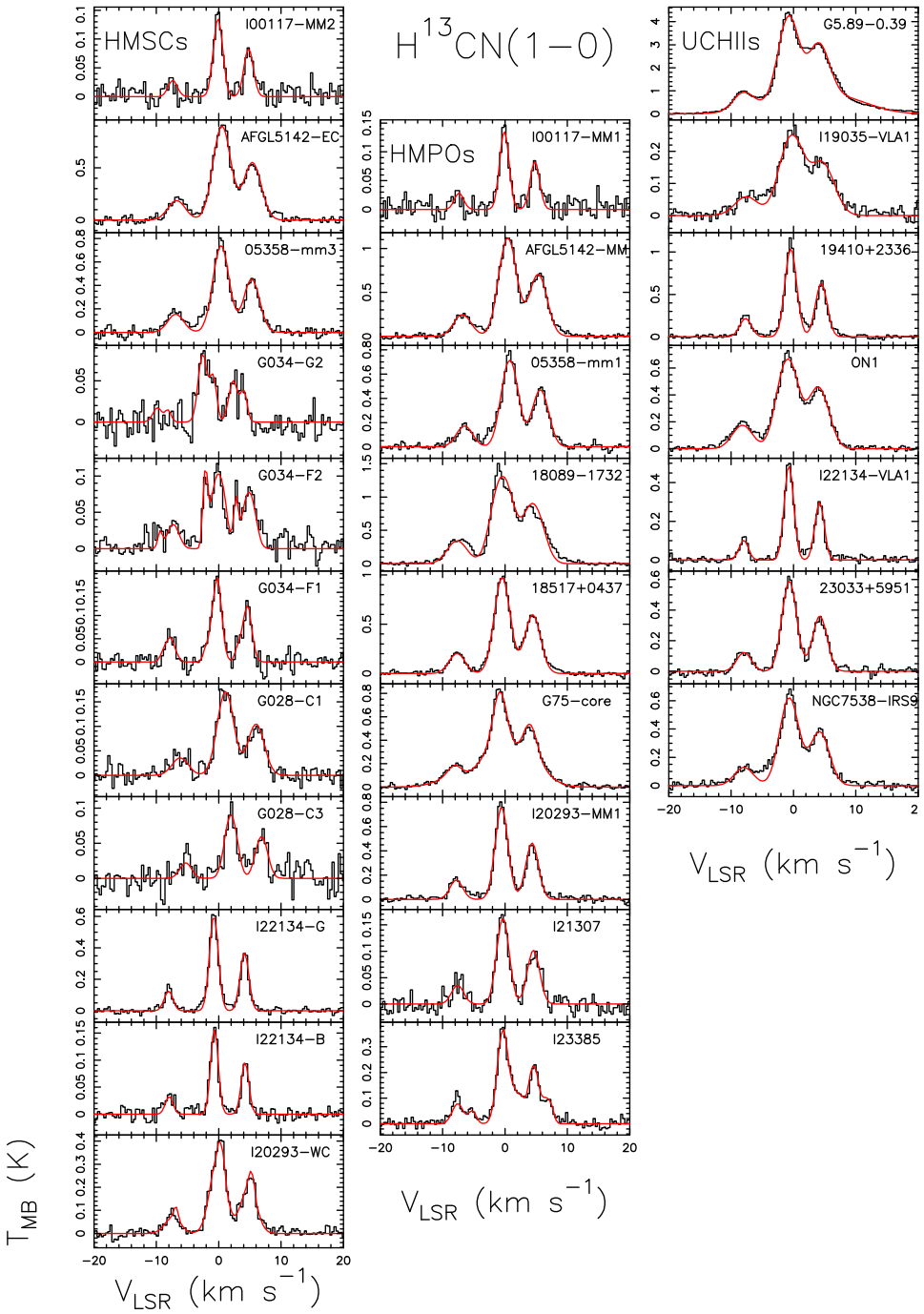

Fig. B.2. Same as Fig.A.3 for $H^{13}CN$(1-0). Here the red curves are the best hyperfine fits obtained with CLASS. Please note the presence of the second velocity component in the same sources indicated in the caption of Fig.B.1.

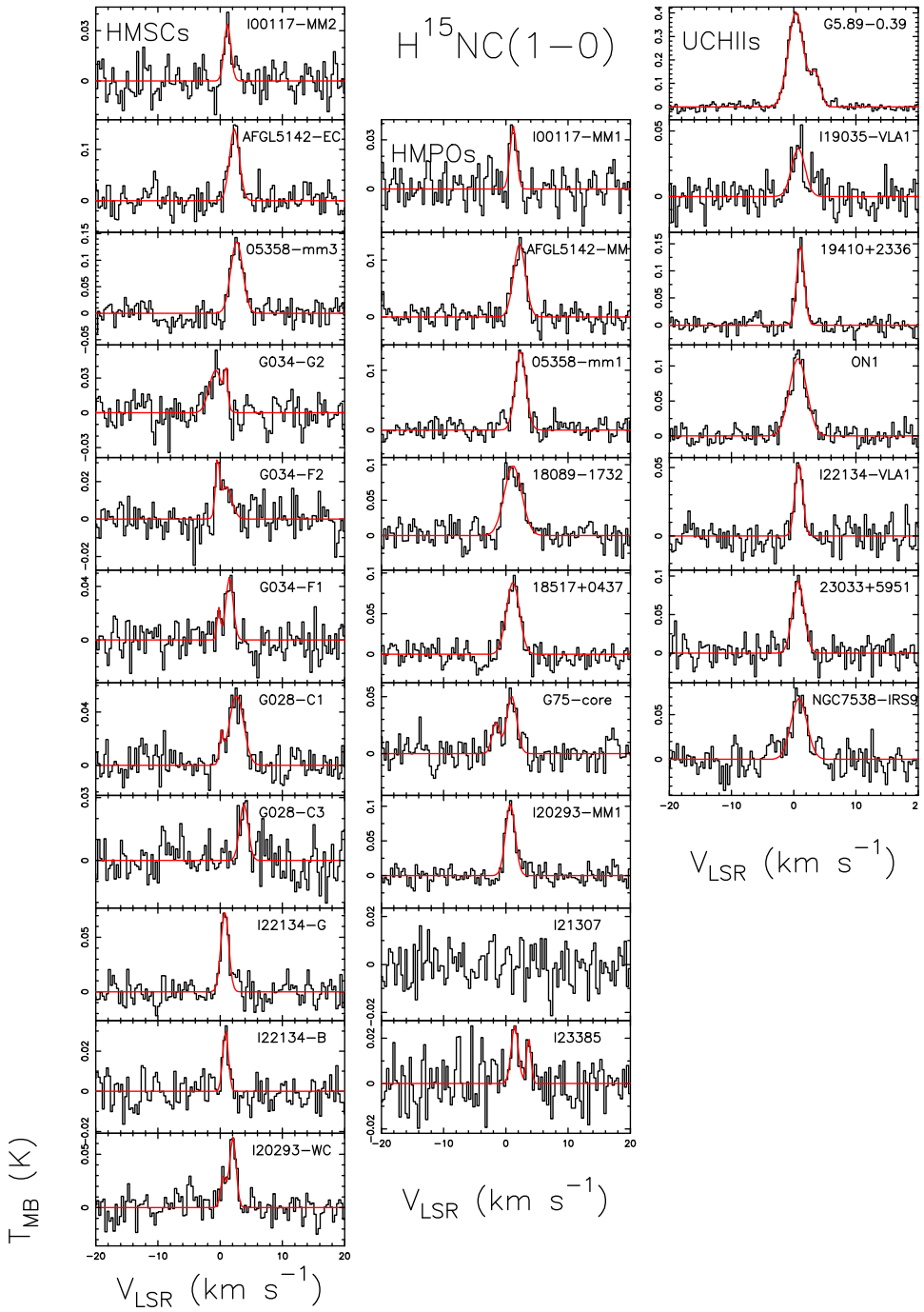

Fig. B.3. Same as Fig.A.3 for $H^{15}NC$(1-0). For I21307 this line was not detected and we have obtained a column density upper limit, as explained in Sect. 3.1.

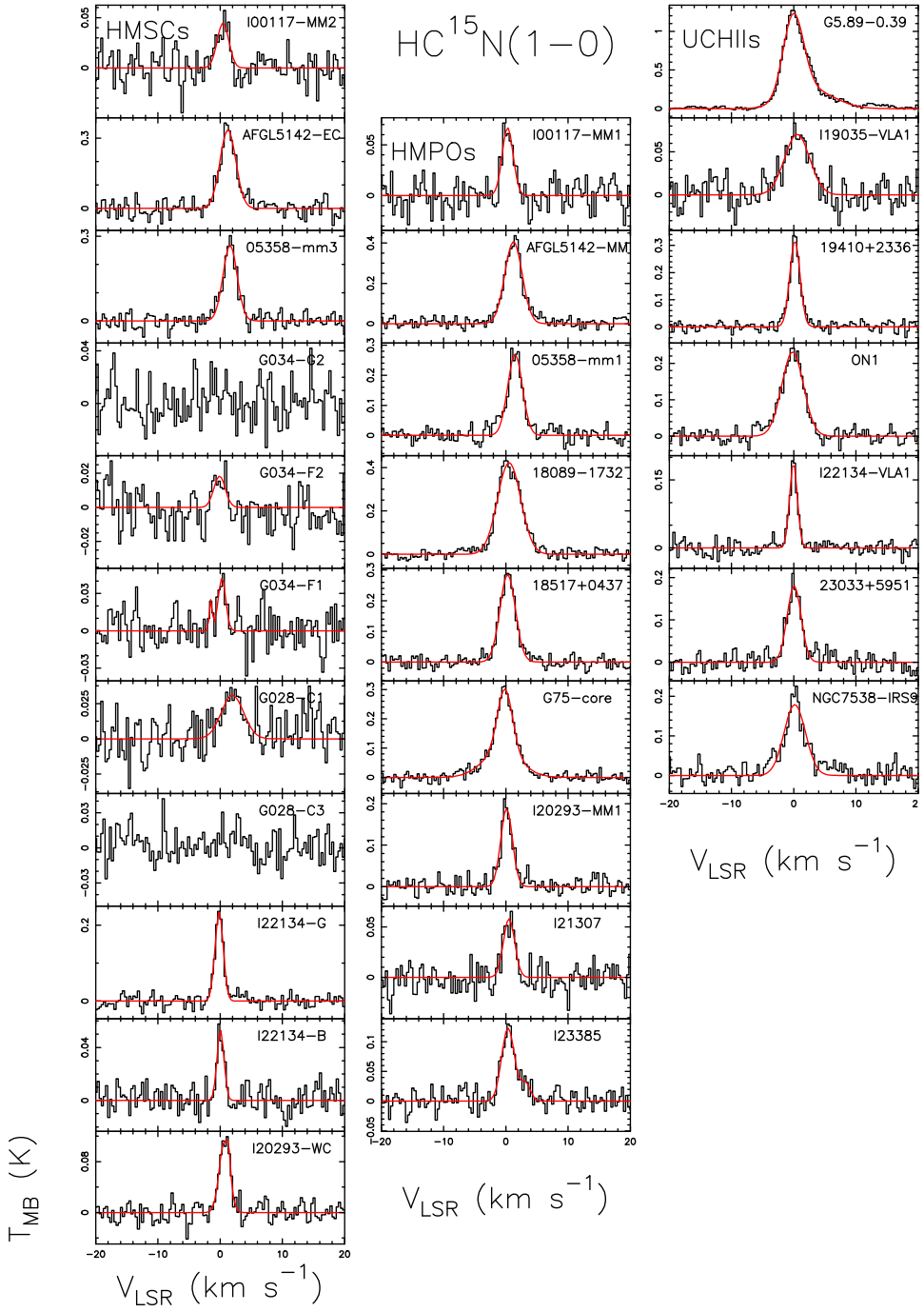

Fig. B.4. Same as Fig.A.3 for $HC^{15}N$(1-0). For G034-G2, G028-C3 and G034-F2 the line was not detected and we obtained a column density upper limit, as explained in Sect. 3.1. For G034-F1 we did not have a clear detection but we have obtained from the Gaussian fit that $T_{MB}^{peak} \gtrsim 2.5\sigma$, we have computed as usual the column density and we refer to this latter as "tentative detection" (see also Table A.2).

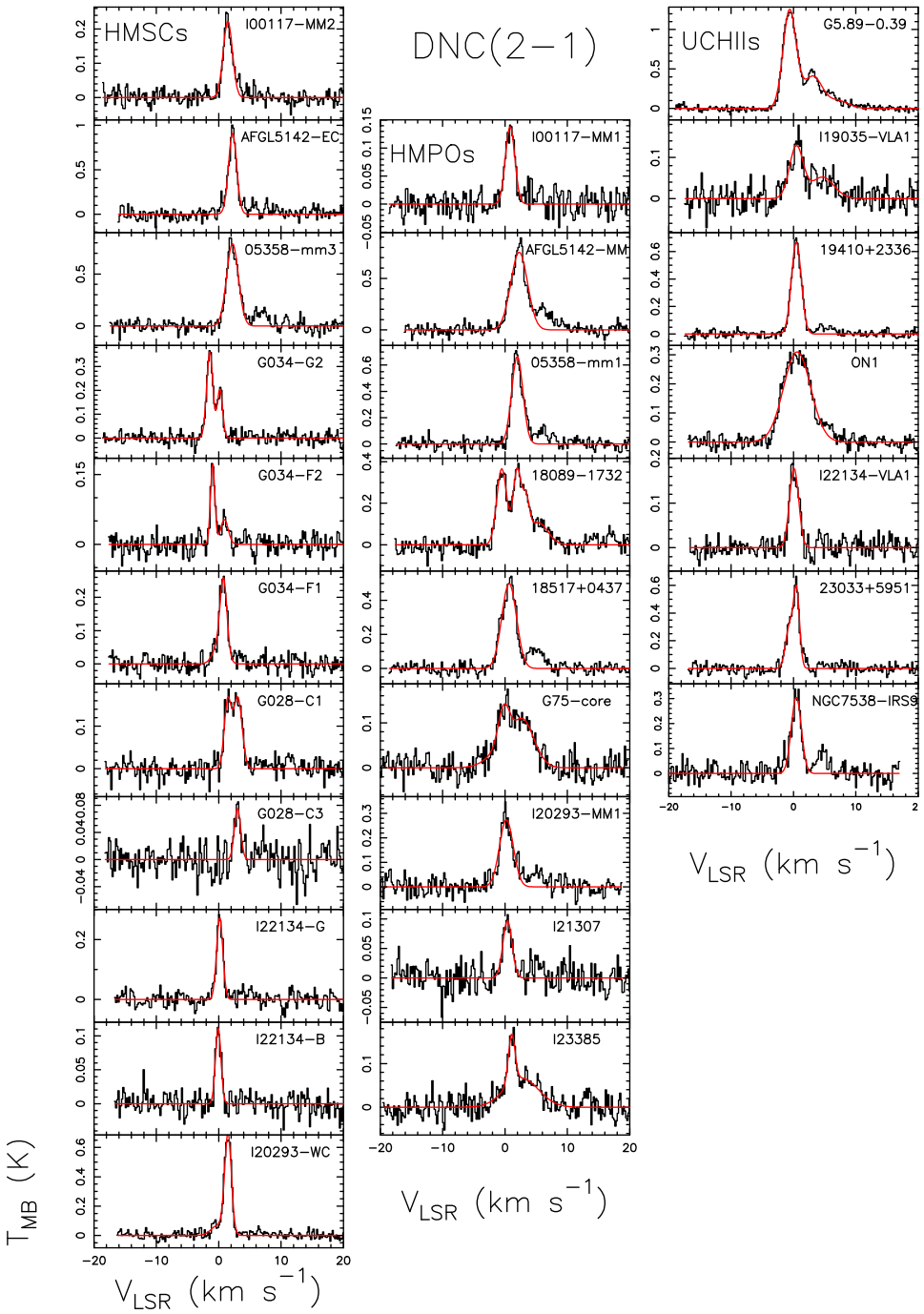

Fig. B.5. Same as Fig.A.3 for DNC(2-1). For evolved sources (HMPOs and UC HII) there is also the acetaldehyde line as explained in Sect. 3.2: when it was possible we have excluded the line from the Gaussian fit, otherwise we have fitted the two lines together and used only the DNC(2-1) to compute the column densities.

Appendix C: Comparison with other molecules

In this appendix, we compare the $^{14}N/^{15}N$ ratios obtained in this paper and in Fontani et al. (2015a) for all the common sources. The $^{12}C/^{13}C$ used and the Galactocentric distances are also listed.

Table C.1. In the second and in the third columns are listed the $^{14}N/^{15}N$ ratios for HNC and HCN found in this work. In the fourth, fifth and sixth columns are listed the $^{14}N/^{15}N$ ratios for N_2H^+ and CN found by Fontani et al. (2015a). In the seventh column are listed the values of $^{12}C/^{13}C$ found from the gradient with the Galactocentric distances given by Milam et al. (2005). In the last column are listed the Galactocentric distances of the sources obtained from the source distance from the Sun (taken from Fontani et al. 2011) and the corresponding galactic longitude.

Source	$\frac{HNC}{H^{15}NC}$	$\frac{HCN}{HC^{15}N}$	$\frac{N_2H^+}{^{15}NNH^+}$	$\frac{N_2H^+}{N^{15}NH^+}$	$\frac{CN}{C^{15}N}$	$\frac{^{12}C}{^{13}C}$	D_{GC} (kpc)
			HMSC				
I00117-MM2	460 ± 80	282 ± 54	670 ± 98	≥ 561	–	69	9.5
AFGL5142-EC	398 ± 39	398 ± 18	1100 ± 360	≥ 1034	330 ± 67	74	10.3
05358-mm3	388 ± 28	433 ± 20	210 ± 12	180 ± 13	400 ± 90	74	10.3
G034-G2(MM2)	365 ± 71	≥ 147	≥ 856	≥ 873	–	50	6.3
G034-F1(MM8)	495 ± 72	369 ± 80	≥ 566	≥ 672	–	47	5.8
G034-F2(MM7)	783 ± 263	≥ 168	≥ 195	≥ 232	–	47	5.8
G028-C1(MM9)	260 ± 30	287 ± 55	≥ 1217	≥ 1445	–	40	4.7
G028-C3(MM11)	338 ± 53	≥ 250	–	–	–	40	4.7
I20293-WC	439 ± 90	620 ± 180	65 ± 69	550 ± 98	–	62	8.3
I22134-G	369 ± 35	322 ± 14	≥ 232	≥ 197	330 ± 150	69	9.5
I22134-B	414 ± 85	406 ± 50	≥ 316	≥ 322	–	69	9.5
			HMPO				
I00117-MM1	388 ± 75	345 ± 38	220 ± 60	≥ 233	≥ 250	69	9.5
AFGL5142-MM	433 ± 27	387 ± 10	740 ± 97	1300 ± 210	190 ± 23	74	10.3
05358-mm1	466 ± 29	432 ± 18	190 ± 20	180 ± 23	240 ± 40	74	10.3
18089-1732	385 ± 204	338 ± 9	1000 ± 400	800 ± 100	450 ± 100	43	5
18517+0437	349 ± 22	326 ± 9	390 ± 53	260 ± 20	310 ± 80	51	6.4
G75-core	554 ± 84	258 ± 3	≥ 209	≥ 240	240 ± 50	63	8.4
I20293-MM1	481 ± 33	504 ± 25	790 ± 67	370 ± 42	–	62	8.3
I21307	≥ 317	389 ± 46	≥ 301	≥ 346	≥ 175	68	9.3
I23385	639 ± 189	290 ± 26	≥ 81	≥ 66	–	81	11.4
			UC HII				
G5.89-0.39	432 ± 10	255 ± 12	320 ± 25	450 ± 51	350 ± 160	55	7.2
I19035-VLA1	570 ± 107	340 ± 27	≥ 572	≥ 754	≥ 270	54	7
19410+2336	431 ± 24	405 ± 12	450 ± 96	500 ± 100	430 ± 250	58	7.7
ON1	467 ± 19	327 ± 8	460 ± 22	350 ± 33	350 ± 220	60	8
I22134-VLA1	364 ± 43	390 ± 18	≥ 80	≥ 108	250 ± 84	69	9.5
23033+5951	397 ± 35	458 ± 21	900 ± 400	700 ± 250	≥ 370	74	10.2
NGC 7538-IRS9	331 ± 37	410 ± 20	≥ 255	≥ 294	230 ± 90	72	9.9